Zerovalent Rh and Ir Silatranes Featuring 2-center, 3-electron Polar Sigma Bonds

Patricia J. Nance, Niklas B. Thompson, Paul H. Oyala, and Jonas C. Peters*

Dedication

Abstract: *Species with 2-center, 3-electron (2c/3e$^-$) σ-bonds are of interest owing to their fascinating electronic structures and potential for interesting reactivity patterns. Herein we report the synthesis and characterization of a pair of zerovalent (d^9) trigonal pyramidal Rh and Ir complexes that feature 2c/3e$^-$ σ-bonds to the Si atom of a tripodal tris(phosphine)silatrane ligand. X-ray diffraction, continuous wave and pulse electron paramagnetic resonance, density functional theory calculations, and reactivity studies have been used to characterize these electronically distinctive compounds. The data available highlight a 2c/3e$^-$ bonding framework with a σ*-SOMO of metal 4- or 5d$_z{}^2$ parentage that is partially stabilized by significant mixing with Si (3p$_z$) and metal (5- or 6p$_z$) orbitals. Metal-ligand covalency thus buffers the expected destabilization of transition metal (TM)-silyl σ*-orbitals via d–p mixing, affording well-characterized examples of TM-to-main group, and hence polar, 2c/3e$^-$ σ "half-bonds".*

First proposed by Linus Pauling almost a century ago, two-center, three-electron (2c/3e$^-$) σ-bonds are still rarely observed. The classic example of these weak "half-bonds" is found in the metastable He_2^+ ion, which houses two electrons in a σ-bonding orbital and a third electron in a σ*-antibonding orbital.[1] Over the years, a limited number of other examples of 2c/3e$^-$ bonds have arisen. For example, unsupported diatomic noble gas monocations and halogen monoanions have been spectroscopically characterized, and structurally characterized in the solid state in the case of Xe_2^+.[2,3] Supported 2c/3e$^-$ bonds have also been the subject of many experimental and theoretical studies, leading to the expansion of this bonding scheme to the pnictogen and chalcogen families (Figure 1a).[4,5,6,7,8] With respect to 2c/3e$^-$ bonds featuring a transition metal (TM), bona fide examples of these bonds have been reported in a fascinating class of homobimetallic, mixed valence Ni_2(II,III) and Pd_2(II,III) paddlewheel complexes, as well as several Fe and Co piano stool dimers.[9,10,11]

Following the spectroscopic characterization of a boron-boron one-electron σ-bond (Figure 1b),[12] our group later reported on a copper-boratrane complex featuring a polar Cu–B 2c/1e$^-$ σ-bond, the first of its type with a TM center (Figure 1b).[13,14] Herein, we describe the extension of this approach towards well-defined 2c/3e$^-$ TM–E σ-half-bonded complexes featuring a TM (Rh or Ir) and a main group element E (Si).[15] Specifically, we report the thorough characterization of zerovalent, d^9 Rh and Ir complexes [K(THF)$_3$][P$_3{}^{Si}$M] (M = Rh, Ir; P$_3{}^{Si}$ = tris(*o*-diisopropylphosphinophenyl)silylide) (Scheme 1). Electron paramagnetic resonance (EPR), density functional theory (DFT) calculations and X-ray structural characterization data highlight their fascinating electronic structures. In particular, the highest-lying σ* SOMO of the 2c/3e$^-$ bond framework is partially stabilized by significant mixing of the 3p$_z$ orbital on the silicon atom of the silatrane ligand with a lobe of metal 4- or 5d$_z{}^2$ parentage. This mixing is manifest via pulse EPR studies.

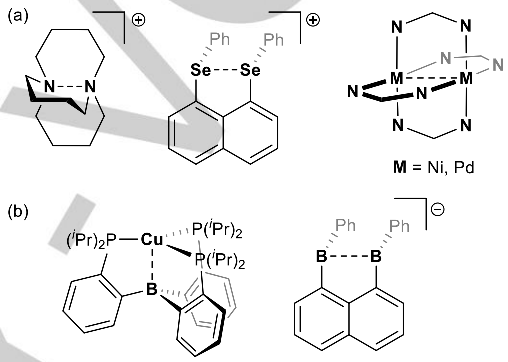

Figure 1. Select examples of supported a) 2-center, 3-electron (**N** = N-(*p*-methoxyphenyl)) and b) 2-center, 1-electron σ-bonds. See text.

One-electron reduction of the previously reported precursors P$_3{}^{Si}$M(N$_2$) (M = Rh (**1**), Ir (**2**)) (Scheme 1)[16,17] at −78 °C afforded access to the zerovalent [K(THF)$_3$][P$_3{}^{Si}$Rh] (**3**) and [K(THF)$_3$][P$_3{}^{Si}$Ir] (**4**) complexes of interest. The cyclic voltammograms of **1** and **2** show quasireversible reduction waves at −3.1 and −3.0 V vs. Fc/Fc$^+$, respectively, necessitating the use of potassium graphite or potassium naphthalenide as the reductant (see SI). Perhaps unsurprisingly, addition of an electron into the 18-electron precursors **1** and **2** causes dissociation of the N$_2$ ligand. Zerovalent Rh and Ir complexes are rather rare, especially for isolable examples.[18,19,20,21]

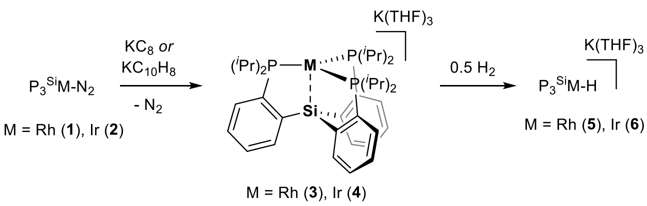

Scheme 1. Synthesis of Rh and Ir complexes **3**-**6**.

Samples of **3** and **4** suitable for X-ray diffraction (XRD) were prepared via recrystallization from a concentrated THF solution layered with chilled pentane, stored at −30 °C. Their solid-state structures, which are shown in Figure 2, were solved in a trigonal crystal system that imposes three equivalent M–P bond distances along with C_3 symmetry about the Si–M–K axis. This symmetry agrees with the symmetry observed in solution via

[*] P. J. Nance, Dr. N. B. Thompson, Dr. P. H. Oyala, Prof. Dr. J. C. Peters
Division of Chemistry and Chemical Engineering
California Institute of Technology
Pasadena CA 91125 (USA)
E-mail: jpeters@caltech.edu

Supporting information for this article is given via a link at the end of the document.

spectroscopy (*vide infra*). The trigonal pyramidal geometry of **3** and **4** is distinctive among the limited number of known zerovalent Rh and Ir complexes, most of which have D_{2d} symmetry.[18,19,20,21,22] For both **3** and **4**, the dihedral angle between the planes formed by P1–M–P2 and P3–M–Si is 90° and the τ_4 value is 86.7, thus showing only minor deviations from an ideal trigonal pyramidal geometry.[23] While the location of the K^+ cations in the solid-state is interesting to consider with respect to possible M–K interactions, such interactions can be easily ruled out *in solution* (see SI).

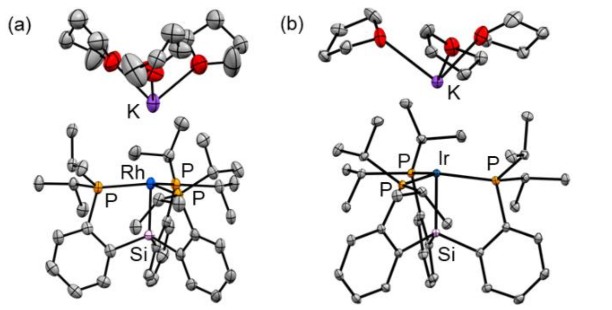

Figure 2. Solid state structures of Rh complex **3** (a) and Ir complex **4** (b). Thermal ellipsoids are depicted at 50% occupancy.

The 77 K X-band continuous wave (CW) EPR spectra of $[P_3^{Si}Rh]^-$ **3** and $[P_3^{Si}Ir]^-$ **4** each give rise to axial signals with $g_\perp > g_\parallel$ ($g_\perp$ is the more intense signal that corresponds to the xy plane of the molecule; $g_\parallel$ corresponds to the unique axis, *z*, oriented parallel to the M-Si bond vector) (Figure 3). Both complexes exhibit anisotropic hyperfine coupling to their corresponding metal nucleus, ^{29}Si, and three equivalent ^{31}P nuclei, implying that the C_3 symmetry observed by XRD is maintained in solution. Metalloradical character is evidenced in the *g* anisotropy (Δg) observed for **3** and **4**, which is larger in the case of the Ir analogue. An increase in metalloradical character is to be expected when moving to a third-row transition metal, as the ligand orbitals mix less with the metal d-orbitals due to poorer energetic overlap that is not sufficiently compensated by increased orbital overlap. In this case, the reduced metal-ligand covalency of **4** should translate to greater localization of the SOMO on the metal center. The large magnitude of the increase in Δg can also be attributed to the greater spin-orbit coupling of Ir.[24]

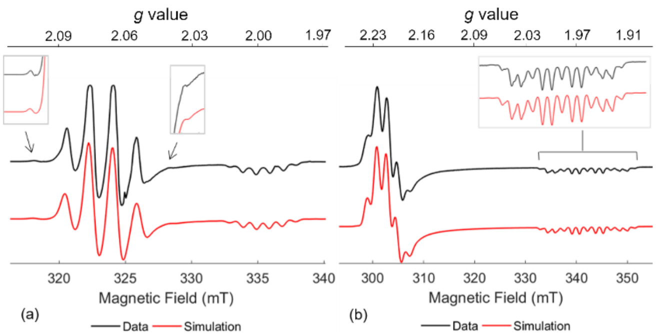

Figure 3. CW X-band EPR spectra at 77 K and corresponding simulations of (a) Rh complex **3** and (b) Ir complex **4**. Insets show (a) satellite peaks and (b) shoulders resulting from ^{29}Si hyperfine coupling.

Table 1. EPR Parameters for Complexes 3 and 4[a]

	Complex	g_x	g_y	g_z
Value	Rh	2.075	2.075	2.000
	Ir	2.208	2.214	1.957
Δg	Rh	0.075	–	–
	Ir	0.25	–	–
$A(^{31}P)$[b]	Rh	52	52	28.5
	Ir	60	60	40
$A(^{29}Si)$	Rh	140	140	170
	Ir	114	114	136
$A(^{103}Rh)$	–	7	7	53
$A(^{191/193}Ir)$	–	20	20	130.5

[a]Hyperfine coupling constants are in MHz. [b]All three ^{31}P nuclei are equivalent.

As an additional tool to probe their electronic structures, Davies electron-nuclear double resonance (ENDOR) spectra were acquired at X-band frequencies (~9.7 GHz) for **3** at 20 K and **4** at 12 K. These data enabled the determination of the ^{31}P, ^{103}Rh, and $^{191/193}Ir$ hyperfine tensors (Table 1). Furthermore, we find that ^{29}Si hyperfine coupling values can be extracted from the ENDOR spectra, which to our knowledge is the first example of such characterization applied to a TM-silyl complex (Figure 4). Corresponding simulations were constrained by fitting the CW X-band spectra of each complex. For both complexes, all coupled nuclei show doublets that are centered at *A*/2 and split by twice their nuclear Larmor frequency (~6 MHz for Si, ~12 MHz for P, <1 MHz for Rh and Ir at X band frequencies), indicative of hyperfine couplings in the strong coupling limit ($A > 2*\nu_I$).[25] The large shift of the Rh and Ir ENDOR signals to higher frequencies as the *g*-value decreases from $g_\perp$ to $g_\parallel$ is suggestive of strong coupling along the principal axis due to the orientation of the spin density relative to the molecular frame. Additionally, hyperfine sublevel correlation (HYSCORE) spectroscopy shows weak coupling to natural abundance ^{13}C that indicates some delocalization of spin density onto the broader ligand platform through noncovalent spin polarization mechanisms (Figure 4, see SI for full data set). The hyperfine tensor associated with this natural abundance ^{13}C coupling was determined to be [3.2, 3.2, 5.8] MHz for **3** and [1.0, 1.0, 5.0] MHz for **4**.

The fact that hyperfine coupling to ^{29}Si (4.7% natural abundance) is sufficiently strong to observe satellite peaks and shoulders in the CW spectra (Figure 3, insets) and ^{29}Si signals in the ENDOR spectra suggests significant contribution of Si orbitals to the SOMOs of **3** and **4**. Decomposition of the ^{29}Si hyperfine tensor of **3** into its isotropic ($a_{iso} = 1/3\ (A_x + A_y + A_z) = 150$ MHz) and anisotropic components ($\mathbf{T} = [(A_x - a_{iso}), (A_y - a_{iso}), (A_z - a_{iso})]$) can be used to estimate the spin density residing in the Si 3s and $3p_z$ orbitals. This process reveals a fully axial anisotropic silicon hyperfine interaction with $\mathbf{T} = [-10, -10, 20]$ MHz. Defining the anisotropic tensor for an electron fully localized in a Si $3p_z$ orbital as $\mathbf{T^0} = [114, 114, -228]$ MHz,[26] spin density in the Si $3p_z$ orbital of **3** is found to be $\rho \sim 0.09$ (or ~9% of an electron). Using $a_{iso}^0 = 4594$ MHz, the Si 3s character in the SOMO is found to be ~3.3%.[26] This analysis was carried out for ^{29}Si, ^{31}P, and the isotropic component of the metal hyperfine coupling and is

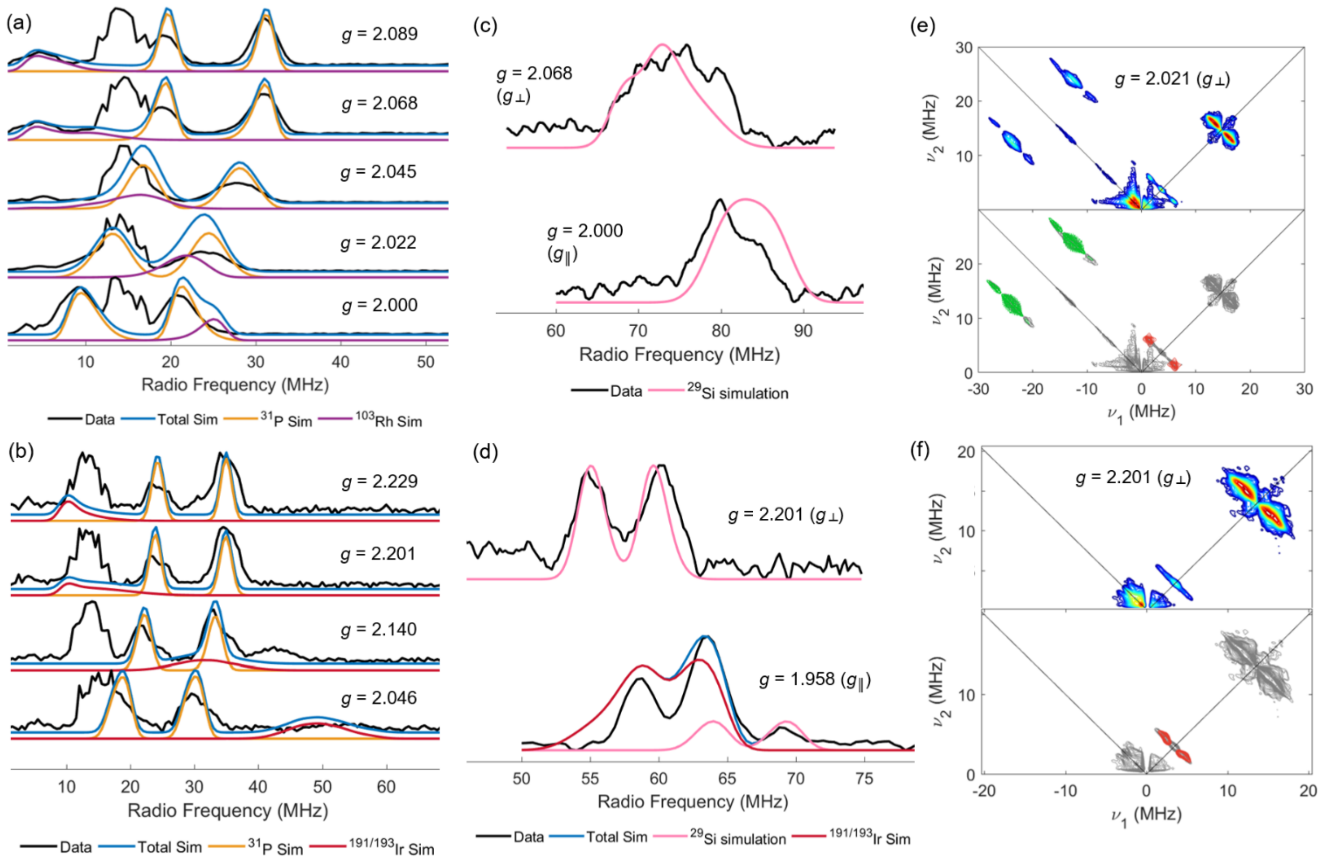

Figure 4. Field-dependent X-band Davies ENDOR and corresponding simulations of (a) complex **3** and (b) complex **4** in the ^{31}P and transition metal coupling region; (c) complex **3** and (d) complex **4** in the ^{29}Si coupling region. (e) X-band HYSCORE spectrum of **3** at *g* = 2.021 (top) and and corresponding simulations (bottom, ^{31}P in green, ^{13}C in red). (f) X-band HYSCORE spectrum of **4** at *g* = 2.201 (top) and corresponding simulations (bottom, ^{13}C in red). See SI for experimental parameters

reported in Table 2. As this method cannot differentiate between spin density in p_z and d_z^2 orbitals, which possess the same axial symmetry, the spin density estimate from the anisotropic component of the metal hyperfine tensor was not calculated.

DFT calculations (TPSSh, second-order DKH scalar relativistic treatment, cc-pVDZ-DK for all atoms except Ir, Si, and P, for which cc-pVTZ-DK was used; single-point calculation performed using nuclear coordinates from crystal structure) were employed to predict hyperfine tensors for the ^{29}Si and ^{31}P atoms of complex **4**. The total ^{29}Si tensor, *A* (^{29}Si), was calculated to be [137, 137, 159] MHz and *A* (^{31}P) was found to be [67, 64, 50] MHz. These values can be compared with those obtained from the CW EPR and ENDOR simulations (*A* (^{29}Si) = [114 114 136]; *A* (^{31}P) = [60 60 40]). The DFT-computed SOMO of **3** (Figure 5) has a_1 symmetry and nicely illustrates the mixing between the axially oriented Si and metal orbitals, as well as the antibonding nature of the interaction.[27] Calculated Löwdin spin populations (Table 2) show that the spin densities of **3** and **4** are primarily metal based (~50% of the unpaired spin on the metal atoms), but with significant delocalization onto the silicon and three equivalent phosphorus atoms. Löwdin reduced orbital spin population analysis quantifies the spin populations of participating orbitals; this shows that metal-based spin is primarily localized within axial orbitals (e.g. 4- or $5d_z^2$ and 5- or $6p_z$) with small isotropic components. The Si $3p_z$ orbitals accommodate most of the spin on Si, while the Si s orbital houses ~2% in both cases. The reduced orbital spin population calculations for Si agree with the spin populations estimated from the breakdown of the experimental hyperfine tensors. As demonstrated experimentally by the Δ*g* values from the CW EPR, DFT calculations predict more metalloradical character for Ir complex **4** than **3**. The remaining ~20% of the spin density for both complexes is delocalized over the rest of the ligand, consistent with the observation of natural abundance ^{13}C signals in the HYSCORE data.

Table 2. Calculated Löwdin Spin Populations and Experimental Spin Density Estimations

	Rh DFT	Rh EPR[b]	Ir DFT	Ir EPR[b]
Metal	48	NC[c]	52	NC
s	5.4	1.8	3.6	1.6
p_z	25	NC	31	NC
d_z^2	18	NC	17	NC
^{29}Si	11	12	8.8	9.0
s	1.7	3.3	1.4	2.6
p_z	7.1	8.8	5.5	6.4
$^{31}P_1$[d]	6.7	2.5	4.3	2.2
s	−0.057	0.33	0.0035	0.40

p_z	2.9	2.1	2.4	1.8

[a]Spin densities are given as percentages. [b]Total spin density estimated from experimental EPR hyperfine coupling is calculated assuming all spin is located in the orbitals included in the Table. [c]*NC = not calculated.* [d]All ^{31}P nuclei are equivalent.

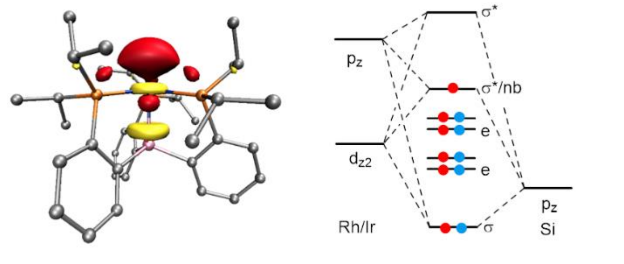

Figure 5. (left) DFT calculated SOMO of $[P_3^{Si}Rh]^-$ (**3**) (isovalue = 0.06 a.u.). (right) Qualitative molecular orbital diagram derived from DFT calculated orbital energies and Löwdin reduced orbital spin population analysis. Parent orbitals involved in M–Si bonding shown on either side.

The occupation of an antibonding orbital with significant silicon character represents a particularly unusual case of a 2c/3e$^-$ σ-bond, as silyl ligands are usually regarded as strongly donating.[28] Such strongly donating ligands might be expected to result in σ* orbitals too destabilized to be populated. The Löwdin reduced orbital spin populations (*vide supra*) give insight into the unusual stability of **3** and **4**. For both complexes, the metal contribution to the SOMO is higher in p_z character than d_z^2 character. This results from symmetry-allowed orbital mixing of the σ* with the (n + 1) s and p_z orbitals of the transition metal. The effect of this mixing has been well-described for both the 2-center, 4-electron case[29] and the 2-center, 3-electron case,[9] as well as in a theoretical study on axial bonding in square planar d^8 ML_4 complexes.[30] Here, such mixing results in decreased destabilization of the σ* orbital (due to increased nonbonding character), and we suggest that the P_3^{Si} ligand platform engenders stability in these unusual zerovalent, 2c/3e$^-$ Rh and Ir complexes by striking a balance between covalency and accessibility of the σ* orbital. The energy of the singly-occupied "antibonding orbital" is significantly buffered by strong metal d_z^2–p_z orbital mixing, thus making the M–Si bond more covalent and allowing the electron density to be shared between the two atoms.

As an additional gauge of the importance of covalency in stabilizing complexes **3** and **4**, the electrochemistry of the corresponding $P_3^{Si}Co(N_2)$ complex was investigated via cyclic voltammetry (see SI). We expected this first-row complex to have the least covalent metal-ligand interactions due to decreased spatial orbital overlap.[31] Indeed, this trend in covalency is observed in a related cationic series $[P_3^{Si}M(PMe_3)][BAr^F_4]$ (M = Co, Rh, Ir; BAr^F_4 = tetrakis[3,5-bis-(trifluoromethyl)phenyl]borate)) of divalent metalloradicals we studied previously.[16] For these, the Δg value of the Co complex (0.61) is significantly larger than that of the Rh and Ir complexes, and the Δg of the Ir complex (0.33) is slightly larger than that of the Rh complex (0.18), presumably due to the decreased energetic overlap of the metal and ligand orbitals and a larger spin-orbit coupling constant. As mentioned above, this same decrease in covalency moving from Rh to Ir is seen in the present system. Because of the irreversibility of the Co(I/0) redox couple, the $E_{p,c}$ of each complex must be compared, rather than the $E_{1/2}$. While the $E_{p,c}$ of the Rh and Ir complexes appear at approximately −3.2 V, the $E_{p,c}$ of the Co analogue shifts cathodically to −3.5 V (scan rate = 100 mV/s). This shift to a significantly more negative potential is consistent with the suggested role of metal-ligand covalency in the stabilization of the present zerovalent Rh and Ir complexes.

The metalloradical character of **3** and **4** observed via EPR and corroborated by DFT calculations is manifest in their reactivity with hydrogen; each reacts cleanly with H_2 to quantitatively generate the corresponding diamagnetic M(I)-hydride $[K(THF)_3][P_3^{Si}M(H)]$ (M = Rh (**5**), Ir (**6**)) (Scheme 1) as products of formal H-atom transfer. These complexes were characterized by ^1H and ^{31}P nuclear magnetic resonance (NMR) spectroscopy and, in the Rh case, XRD analysis (Figure 6). Despite having a similar structure to **3**, the hydride position of **5** was located in the difference map, and the Rh–K distance increases by over 0.5 Å (see SI for bond metrics). The ^1H NMR hydride resonance shown for **5** resembles a quintet, resulting from overlap of a doublet of quartets via coupling of one Rh center and three equivalent P nuclei. This was confirmed by a $^1H\{^{31}P\}$ NMR spectrum, in which the hydride peak is a doublet. The reactivity of **3** and **4** with H_2 is reminiscent of R-H (R = H, alkyl) activations by classic Rh(II) porphyrin metalloradicals.[32]

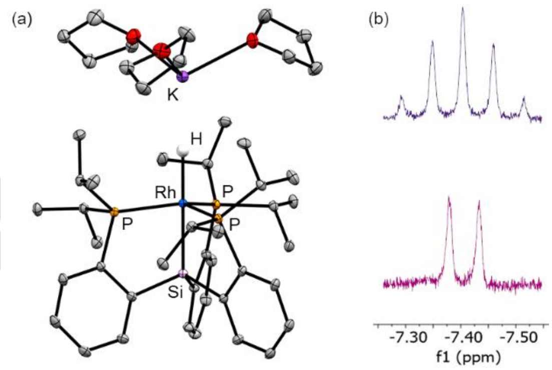

Figure 6. (a) Solid state structure of Rh(I)–H **5** derived from H-atom abstraction reactions. Thermal ellipsoids are shown at 50% probability. H atoms (other than the hydride ligand) are omitted for clarity. (b) ^1H NMR (top) and $^1H\{^{31}P\}$ NMR (bottom) of the hydride signal for Rh–H **5**.

To close, the synthesis, isolation, and characterization of zerovalent Rh and Ir complexes bearing 2c/3e$^-$ M–Si bonds has been described. The proposed electronic structure of these complexes, supported by CW and pulse EPR measurements, as well as DFT calculations, are defined by SOMOs that are primarily metal based and considerably stabilized by strong TM d_z^2–p_z orbital mixing. This mixing places substantial spin density on the silicon atom of the silatrane ligand, evinced by ^{29}Si ENDOR spectroscopy. The degree of silicon character in the σ*-SOMOs is unusual for TM-silyl complexes, as silyl ligands are strong σ-donors that lead to highly destabilized antibonding orbitals. Herein, the metal-ligand covalency and buffered destabilization of the σ*-orbitals from d–p mixing lead to a rarely observed bonding scheme for a TM-silyl complex.

Acknowledgements

We are grateful for funding from the Department of Energy (DOE-0235032), from the NSF via its MRI program (NSF-1531940) in support of the Caltech EPR facility, and to the DOW Next Generation Educator Fund. PJN is grateful for an NSF GRF. We also thank Dr. Michael Takase and Larry Henling for assistance with X-ray crystallography.

Keywords: 2-center, 3-electron bonding • Hydrogen Cleavage • Metalloradical • Zerovalent Rhodium • Zerovalent Iridium

[1] Pauling, L. *J. Am. Chem. Soc.* **1931**, *53*, 3225–3237.
[2] Castner, T. G.; Känzig, W. *J. Phys. Chem. Solids* **1957**, *3*, 178–195.
[3] Drews, T.; Seppelt, K. *Angew. Chem. Int. Ed.* **1997**, *36*, 273–274.
[4] Braïda, B.; Thogersen, L.; Wu, W.; Hiberty, P. C. *J. Am. Chem. Soc.* **2002**, *124*, 11781–11790.
[5] Alder, R. W. *Tetrahedron* **1990**, *46*, 683–713.
[6] Gerson, F.; Knoebel, J.; Buser, U.; Vogel, E.; Zehnder, M. *J. Am. Chem. Soc.* **1986**, *108*, 3781–3783.
[7] Zhang, S.; Wang, X.; Su, Y.; Qiu, Y.; Zhang, Z.; Wang, X. *Nat. Commun.* **2014**, *5*, 4127.
[8] Zhang, S.; Wang, X.; Sui, Y.; Wang, X. *J. Am. Chem. Soc.* **2014**, *136*, 14666–14669.
[9] Berry, J. F. *Acc. Chem. Res.* **2016**, *49,* 27–34 and references therein.
[10] Dahl, L. F.; Connelly, N. G. *J. Am. Chem. Soc.* **1970**, *92*, 7472–7474.
[11] Zheng, X.; Wang, X.; Zhang, Z.; Sui, Y.; Wang, X.; Power, P. P. *Angew. Chem. Int. Ed.* **2015**, *54*, 9084–9087.
[12] (a) Hofelmeyer, J. D.; Gabbai, F. P. *J. Am. Chem. Soc.* **2000**, *122*, 9054–9055. (b) Hübner, A.; Diehl, A. M.; Diefenbach, M.; Endeward, B.; Bolte, M.; Lerner, H.-W.; Holthausen, M. C.; Wagner, M. *Angew. Chem. Int. Ed.* **2014**, *53*, 4832–4835.
[13] Moret, M.-E.; Zhang, L.; Peters, J. C. *J. Am. Chem. Soc.* **2013**, *135*, 3792–3795.
[14] For select recent references related to 2c/1e$^-$ sigma bonds, see: (a) Mierzwa, G.; Gordon, A.; Berski, S. *New J. Chem.* **2018**, *42*, 17096-17114. (b) Oliveira de Sousa, D. W.; Chaer, N.; Marco, A. *Acc. Chem. Res*. **2017**, *50*, 2264-2272. (c) Kusevska, E.; Montero-Campillo, M. M.; Mo, O.; Yanez, M. *Angew. Chem. Int. Ed.* **2017**, *56*, 6788–6792.
[15] For recently reported complexes featuring 2c/3e$^-$-bonding between Ni-Al/Ga, where the three valence electrons are assigned to bonding orbitals, see: Vollmer, M. W.; Xie, J.; Cammarota, R. C.; Young, V. G.; Bill, E.; Gagliardi, L.; Lu, C. C. *Angew. Chem. Int. Ed.* **2018**, *57*, 7815–7819.
[16] Takaoka, A.; Peters, J. C. *Inorg. Chem.* **2012**, *51*, 16–18.
[17] Whited, M. T.; Mankad, N. P.; Lee, Y.; Oblad, P. F.; Peters, J. C. *Inorg. Chem.* **2009**, *48*, 2507–2517.
[18] Boulmaâz, S.; Loss, S.; Schönberg, H.; Deblon, S.; Wörle, M.; Nesper, R.; Grützmacher, H.; Mlakar, M. *Chem. Commun.* **1998**, *23*, 2623–2624.
[19] Longato, B.; Coppo, R.; Pilloni, G.; Corvaja, C.; Toffoletti, A.; Bandoli, G. *J. Organomet. Chem.* **2001**, *637–639*, 710–718.
[20] Longato, B.; Riello, L.; Bandoli, G.; Pilloni, G. *Inorg. Chem.* **1999**, *38*, 2818–2823.
[21] Schönberg, H.; Boulmaâz, S.; Wörle, M.; Liesum, L.; Schweiger, A.; Grützmacher, H. *Angew. Chem. Int. Ed.* **1998**, *37*, 1423–1426.
[22] de Bruin, B.; Russcher, J. C.; Grützmacher, H. *J. Organomet. Chem.* **2007**, *692*, 3167–3173.
[23] Yang, L.; Powell, D. R.; Houser, R. P. *Dalton Trans.* **2007**, *9*, 955–964.
[24] de Bruin, B.; Hetterscheid, D. G. H.; Koekkoek, A. J. J.; Grützmacher, H. *Prog. Inorg. Chem*. **2007**, *55*, 247.
[25] Schweiger, A.; Jeschke, G. *Principles of Pulse Electron Paramagnetic Resonance.* Oxford University Press: New York, 2001.
[26] Morton, J. R.; Preston, K. F. *J. Magn. Reson.* **1978**, *30*, 577–582.
[27] DFT parameters in brief: TPSS, ZORA relativistic effect treatment, def2-svp on all atoms except Rh, Ir (def2-qzvp) and Si, P (def2-tzvp). Geometry optimization performed from nuclear coordinates obtained via XRD.
[28] Tilley, T. D. Transition-Metal Silyl Derivatives. In *The Silicon–Heteroatom Bond*; J. Wiley, 1991; pp 245–308.
[29] Bercaw, J. E.; Durrell, A. C.; Gray, H. B.; Green, J. C.; Hazari, N.; Labinger, J. A.; Winkler, J. R. *Inorg. Chem.* **2010**, *49*, 1801–1810.
[30] Aullón, G.; Alvarez, S. *Inorg. Chem.* **1996**, *35*, 3137-3144.
[31] Housecroft, C. E.; Sharpe, A. G. *Inorganic Chemistry*, 4th ed.; Pearson: Harlow, 2012.
[32] Wayland, B.B.; Ba, S.; Sherry, A. E. *Inorg. Chem.*, **1992**, *31*, 148–150.

Entry for the Table of Contents (Please choose one layout)

Layout 2:

COMMUNICATION

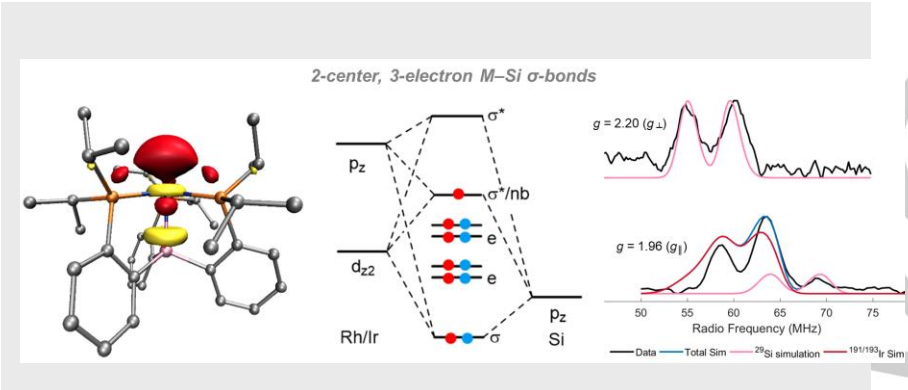

*P. J. Nance, Dr. N. B. Thompson, Dr. P. H. Oyala, and Prof. Dr. J. C. Peters**

Page No. – Page No.

Zerovalent Rh and Ir Silatranes Featuring 2-center, 3-electron Polar Sigma Bonds

Species with 2-center, 3-electron (2c/3e$^-$) σ-bonds are of interest owing to their fascinating electronic structures and reactivity patterns. Herein we report on a pair of zerovalent (d^9) trigonal pyramidal Rh and Ir silatranes featuring 2c/3e$^-$ σ-bonds. Structural, spectroscopic, and theoretical data indicate that metal-ligand covalency buffers the expected destabilization of their transition metal (TM)-silyl σ*-orbitals via d-p mixing, thereby affording distinct examples of polar TM-main group 2c/3e$^-$ σ "half bonds".

Table of Contents

Experimental Methods

General considerations. All manipulations were carried out using standard Schlenk or glovebox techniques under an N_2 atmosphere. Unless otherwise noted, solvents were deoxygenated and dried by thoroughly sparging with N_2 gas followed by passage through an activated alumina column in the solvent purification system by SG Water, USA LLC. Solvents were tested with a standard purple solution of sodium benzophenone ketyl in tetrahydrofuran in order to confirm effective moisture removal. All reagents were purchased from commercial vendors and used without further purification unless otherwise stated. The compounds tris(*o*-diisopropylphosphinophenyl)silane) (HP_3^{Si}),[1] $P_3^{Si}Rh(H)(Cl)$[2], $P_3^{Si}Ir(H)(Cl)$[1], $P_3^{Si}Rh(N_2)$,[1] $P_3^{Si}Ir(N_2)$,[1] and KC_8[3] were synthesized following literature procedures. Deuterated solvents were purchased from Cambridge Isotope Laboratories, Inc., degassed and stored over activated 3 Å molecular sieves prior to use.

Physical methods. NMR data were collected on a Varian 400 MHz instrument with chemical shifts reported in ppm relative to C_6D_6 or THF-d_8, using residual solvent resonances as internal standards. ^{31}P chemical shifts are reported in ppm relative to 85% aqueous H_3PO_4. Electrochemical measurements were carried out in a glovebox under an N_2 atmosphere in a one compartment cell using a CH Instruments 600B electrochemical analyzer. A glassy carbon electrode was used as the working electrode and a platinum wire was used as the auxiliary electrode. A silver pseudoreference electrode was used with the ferrocene couple (Fc/Fc^+) as an internal reference, unless otherwise noted. Solutions of electrolyte (0.2 M [TBA][PF_6] in THF) and analyte were also prepared under an N_2 atmosphere. Thin film IR spectra were obtained using a Bruker Alpha Platinum ATR spectrometer with OPUS software in a glovebox under an N_2 atmosphere. Elemental analyses were performed by the Beckman Institute Crystallography Facility (Caltech).

DFT calculations. Optimization and frequency calculations were performed using version 3.0.3 of the ORCA package.[4] Single-point hyperfine coupling calculations for **4** (using coordinates from X-ray diffraction) were carried out using version 4.0.1.2 of the ORCA package.[5] Structures of **3** and **4** were optimized using the crystal structure coordinates as the input. For optimization and frequency calculations, the TPSS functional was used with the def2-QZVP basis set on Rh/Ir, the def2-TZVP basis set on Si and P, and the def2-SVP basis set on all other atoms. The ZORA scalar relativistic Hamiltonian was employed. For the hyperfine coupling calculation, the TPSSh functional was used with the cc-pVTZ-DK basis set on Ir, Si and P, and the cc-pVDZ-DK basis set on all other atoms. The second-order DKH scalar relativistic Hamiltonian was used.

X-ray diffraction. X-ray diffraction measurements were carried out in the Beckman Institute Crystallography Facility. XRD measurements were collected using a dual source Bruker D8 Venture, four-circle diffractometer with a PHOTON CMOS detector (Mo Kα or Cu Kα radiation). Structures were solved using SHELXT and refined against F_2 on all data by full-matrix least squares with SHELXL. The crystals were mounted on a glass fiber under Paratone N oil.

CW EPR spectroscopy. X-band (9.4 GHz) CW EPR spectra were acquired using a Bruker EMX spectrometer equipped with a Super High-Q (SHQE) resonator using Bruker Win-EPR software (ver. 3.0). Spectra were acquired at 77 using a vacuum-insulated quartz liquid nitrogen immersion dewar inserted into the EPR resonator. Spectra were simulated using the EasySpin simulation toolbox (release 5.2.15) with Matlab R2016b.[6]

Pulse EPR spectroscopy. All pulse X-band (9.7 GHz) hyperfine sublevel correlation (HYSCORE) and electron nuclear double resonance (ENDOR) spectra were acquired using a Bruker ELEXSYS E580 pulse EPR spectrometer equipped with a Bruker MD4 resonator. Temperature control was achieved using an ER 4118HV-CF5-L Flexline Cryogen-Free VT cryostat manufactured by ColdEdge equipped with an Oxford Instruments Mercury ITC temperature controller.

Electron spin-echo detected EPR (ESE-EPR) field-swept spectra were acquired using the 2-pulse "Hahn-echo" sequence ($\pi/2 - \tau - \pi - \tau -$ echo) where τ was held constant. Subsequently, each field swept echo-detected EPR absorption spectrum was modified using a pseudo-modulation function to approximate the effect of field modulation and produce the CW-like 1st derivative spectrum.[7]

Pulse X-band HYSCORE spectra were acquired using the 4-pulse sequence ($\pi/2 - \tau - \pi/2 - t_1 - \pi - t_2 - \pi/2 - \tau -$ echo), where τ is a fixed delay, and t_1 and t_2 are variable delays independently incremented by Δt_1 and Δt_2, respectively. Sixteen step phase cycling was utilized. The time domain spectra were baseline-corrected (third-order polynomial), apodized with a Hamming window function, zero-filled to eight-fold points, and fast Fourier-transformed to yield the frequency domain.

Pulse X-band ENDOR spectra were acquired using the Davies pulse sequence ($\pi - t_{RF} - \pi_{RF} - t_{RF} - \pi/2 - \tau - \pi -$ echo), where t_{RF} is the delay between MW pulses and RF pulses, π_{RF} is the length of the RF pulse. For all lower-frequency ENDOR data (Figure 4a,b in the main text), π = 80 ns, t_{RF} = 2 μs, π_{RF} = 15 μs, τ = 350 ns shot repetition time (srt.) = 5 ms. For all ^{29}Si ENDOR data (Figure 4b,c main text), π = 80 ns, t_{RF} = 2 μs, π_{RF} = 45 μs, τ = 350 ns shot repetition time (srt.) = 5 ms. The RF frequency was randomly sampled during each pulse sequence. ^{29}Si ENDOR were smoothed using a 3-point Savitzky-Golay filter for Ir complex **4** and a 5-point Savitzky-Golay filter for Rh complex **3**.

In general, the ENDOR spectrum for a given nucleus with spin I= ½ (^{1}H) coupled to the S = ½ electron spin exhibits a doublet at frequencies

$$\nu_{\pm} = \left|\frac{A}{2} \pm \nu_N\right| \tag{1}$$

Where ν_N is the nuclear Larmor frequency and A is the hyperfine coupling. For nuclei with $I \geq 1$ (^{14}N, ^{2}H), an additional splitting of the $\nu_{\pm}$ manifolds is produced by the nuclear quadrupole interaction (P)

$$\nu_{\pm,m_I} = \left|\nu_N \pm \frac{3P(2m_I - 1)}{2}\right| \tag{2}$$

In HYSCORE spectra, these signals manifest as cross-peaks or ridges in the 2-D frequency spectrum which are generally symmetric about the diagonal of a given quadrant. This technique allows hyperfine levels corresponding to the same electron-nuclear submanifold to be differentiated, as well as separating features from hyperfine couplings in the weak-coupling regime

($|A| < 2|\nu_I|$) in the (+,-) quadrant from those in the strong coupling regime ($|A| > 2|\nu_I|$) in the (-,-) quadrant. The (-,-) and (+,-) quadrants of these frequency spectra are symmetric to the (+,+) and (-,+) quadrants, thus typically only two of the quadrants are typically displayed in literature. For systems with appreciable hyperfine anisotropy in frozen solutions or solids, HYSCORE spectra typically do not exhibit sharp cross peaks, but show ridges that represent the sum of cross peaks from selected orientations at the magnetic field position at which the spectrum is collected. The length and curvature of these correlation ridges allow for the separation and estimation of the magnitude of the isotropic and dipolar components of the hyperfine tensor, as shown in Figure S1.

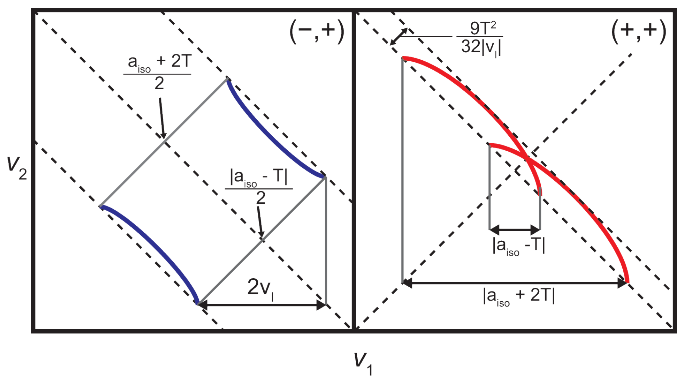

Figure S1. HYSCORE powder patterns for an $S = 1/2$, $I = 1/2$ spin system with an axial hyperfine tensor which contains isotropic (a_{iso}) and dipolar (T) contributions. Blue correlation ridges represent the strong coupling case; red correlation ridges represent the weak coupling case.

Synthesis and characterization of compounds 3 – 6

[K(THF)$_3$][P_3^{Si}*Rh] (**3**).* $P_3^{Si}Rh(N_2)$ (25 mg) was dissolved in 1 mL THF. Excess KC_8 (approximately 2 mm layer) was placed in a Pasteur pipette plugged with filter paper. Both were cooled to −78 °C. The $P_3^{Si}Rh(N_2)$ was filtered through the KC_8 filled pipette to give dark green-brown [K(THF)$_3$][SiP$^{iPr}_3$Rh]. Layering approximately 3 mL of chilled pentane over the THF solution and storing at −30 °C yielded crystals suitable for XRD analysis. The crude reaction solution mixture shows a small impurity of the diamagnetic side-product *[K(THF)$_3$][*P_3^{Si}*Rh-H)]* ***5*** by NMR spectroscopy. Spectroscopically pure material could be isolated in 37% yield by recrystallization from a THF/pentane mixture. ^{1}H NMR (400 MHz, d$_8$-THF, 295 K, ppm): δ 6.9, 4.9, −0.4, −1.8. UV-vis (THF) λ_{max}, nm (ε, M^{-1} cm^{-1}): 630 (3100), 710 (2500). Anal. Calcd.: C, 59.67; H, 8.15; N. 0.00. Found: C, 58.07; H, 8.12; N, 0.26.

[K(THF)$_3$][P_3^{Si}*Ir] (4).* $P_3^{Si}Ir(N_2)$ (25 mg) was dissolved in 1 mL THF. Excess KC_8 (approximately 2 mm layer) was placed in a Pasteur pipette plugged with filter paper. Both were cooled to −78 °C. The $P_3^{Si}Ir(N_2)$ was filtered through the KC_8 filled pipette to give dark green-brown [K(THF)$_3$][P_3^{Si}Ir]. Layering approximately 3 mL of chilled pentane over the THF solution and storing at −30 °C yielded crystals suitable for XRD analysis. As for **3**, the crude reaction solution mixture shows a small impurity of diamagnetic *[K(THF)$_3$][*P_3^{Si}*Ir-H)]* ***6*** by NMR analysis.

Spectroscopically pure material was isolated in 56% yield by recrystallization from a THF/pentane mixture. ^{1}H NMR (400 MHz, d$_8$-THF, 295 K, ppm): δ 27.6, 16.1, 9.7, 8.8, 2.2. UV-vis (THF) λ_{max}, nm (ε, M^{-1} cm^{-1}): 360 (11050), 580 (3600) 708 (1800). Anal. Calcd.: C, 54.60; H, 7.46; N. 0.00. Found: C, 54.24; H, 7.55; N, 0.21.

*[K(THF)$_3$][SiP$^{iPr}{}_3$Rh–H] (**5**).* [K(THF)$_3$][P$_3^{Si}$Rh] (10 mg) was dissolved in THF (< 1 mL) and the solution was added to a J. Young NMR tube. The solution was subjected to three freeze-pump-thaw cycles. H_2 was flowed slowly through a liquid nitrogen cooled trap to dry before it was added to the evacuated sample tube. The J. Young tube was inverted repeatedly and the solution changed from dark greenish brown to red over the course of 5 minutes. The transformation was quantitative by NMR analysis (^{1}H and ^{31}P). Layering the THF solution with 3 mL of pentane and storing at room temperature yielded crystals suitable for XRD analysis.

Alternate synthesis: P$_3^{Si}$Rh(H)(Cl) (30 mg, 0.067 mmol) was dissolved in THF and cooled to −78 °C. Excess KC$_8$ (approximately 2 mm layer) was placed in a Pasteur pipette plugged with filter paper. The solution of P$_3^{Si}$Rh(H)(Cl) was passed over the KC$_8$ several times. By this method, some Rh–N$_2$ complex **1** is formed as a byproduct; thus, the solution was concentrated and layered with 3 mL pentane to give spectroscopically pure material in 47% yield.

^{1}H NMR (400 MHz, d$_8$-THF, 295 K, ppm): δ 8.07 (d, J = 7.0 Hz, Ar-C*H*, 3H) , 7.24 (d, J = 7.4 Hz, Ar-C*H*, 3H), 6.95 (t, J = 7 Hz, Ar-C*H*, 3H), 6.83 (t, J = 7 Hz, Ar-C*H*, 3H), 1.96 (br, -C*H*(CH$_3$)$_2$, 6H), 0.80 (br, -CH(C*H*$_3$)$_2$, 18H), 0.47 (br, -CH(C*H*$_3$)$_2$, 18H), −7.40 (dq, J_{Rh-H} = 43 Hz, J_{P-H} = 22 Hz, Rh-*H*, 1H). ^{31}P{^{1}H} (162 MHz, d$_8$-THF, 295 K, ppm): δ 75.89 (d). IR (solid, cm^{-1}): 1614 (Rh–H, broad). Combustion analysis was attempted two times but was invariably low in carbon, which we presume to be due to the retention of salt that is difficult to separate.

*[K(THF)$_3$][SiP$^{iPr}{}_3$Ir–H] (**6**).* [K(THF)$_3$][P$_3^{Si}$Ir] (10 mg) was dissolved in THF (< 1 mL) and the solution was added to a J. Young NMR tube. The solution was subjected to three freeze-pump-thaw cycles. H_2 was flowed slowly through a liquid nitrogen cooled trap to dry before it was added to the evacuated sample tube. The J. Young tube was inverted repeatedly and the solution changed from dark greenish brown to red over the course of 5 minutes. The transformation was quantitative by NMR analysis (^{1}H and ^{31}P). Layering the THF solution with 3 mL of pentane and storing at room temperature yielded crystals suitable for XRD analysis.

Alternate synthesis: P$_3^{Si}$Ir(H)(Cl) (30 mg, 0.067 mmol) was dissolved in THF and cooled to −78 °C. Excess KC$_8$ (approximately 2 mm layer) was placed in a Pasteur pipette plugged with filter paper. The solution of P$_3^{Si}$Ir(H)(Cl) was passed over the KC$_8$ several times, turning a vibrant orange. This was repeated until the color stopped getting progressively darker. The solution was concentrated under vacuum. The solid was washed with pentane to give **6** in 93% yield.

^{1}H NMR (400 MHz, d$_8$-THF, 295 K, ppm): δ 8.09 (d, J = 7.0 Hz, Ar-C*H*, 3H) , 7.18 (d, J = 7.3 Hz, Ar-C*H*, 3H), 6.87 (t, J = 7.0 Hz, Ar-C*H*, 3H), 6.74 (t, J = 7.2 Hz, Ar-C*H*, 3H), 1.84 (br, -C*H*(CH$_3$)$_2$, 6H), 0.75 (br, -CH(C*H*$_3$)$_2$, 18H), 0.46 (br, -CH(C*H*$_3$)$_2$, 18H), −11.37 (q, J = 18, Ir-*H*, 1H). ^{31}P{^{1}H} (162 MHz, d$_8$-THF, 295 K, ppm): δ 50.53 (s). IR (solid, cm^{-1}): 1774 (Ir–H, broad). Combustion analysis was attempted three times but was invariably low in carbon, which we presume (as for **5**) to be due to the retention of salt that is difficult to separate.

NMR spectra

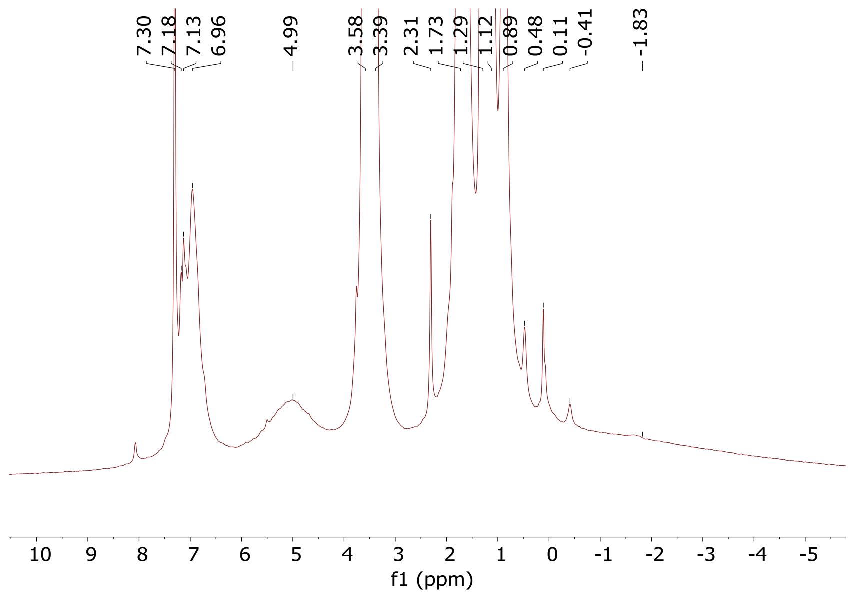

Figure S2. ^{1}H NMR (400 MHz, d_8-THF, 295 K) spectrum of Rh complex **3**. Diamagnetic peaks are from THF, pentane, benzene, toluene, and diethyl ether. Small peaks at 8.0 and 0.48 ppm are from a small amount of Rh–H **5**, which results from the slow reaction of **3** with THF solvent.

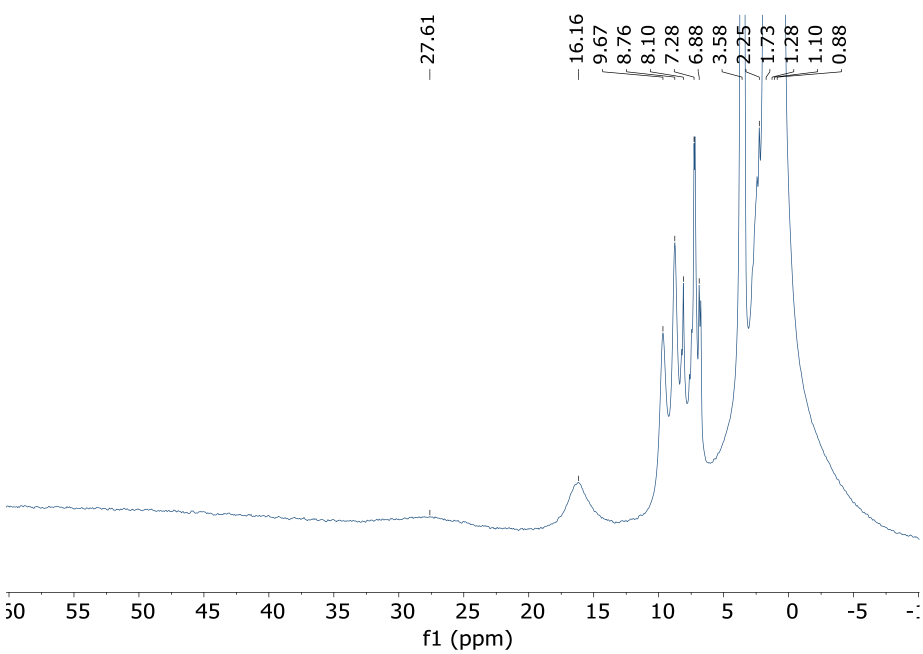

Figure S3. ^{1}H NMR (400 MHz, d_8-THF, 295 K, ppm) spectrum of Ir complex **4**. Diamagnetic peaks are from THF, pentane, and benzene. Sharp peaks at 8.10 and 6.88 ppm are from a small amount of Ir–H **6**, which results from the slow reaction of **4** with THF solvent.

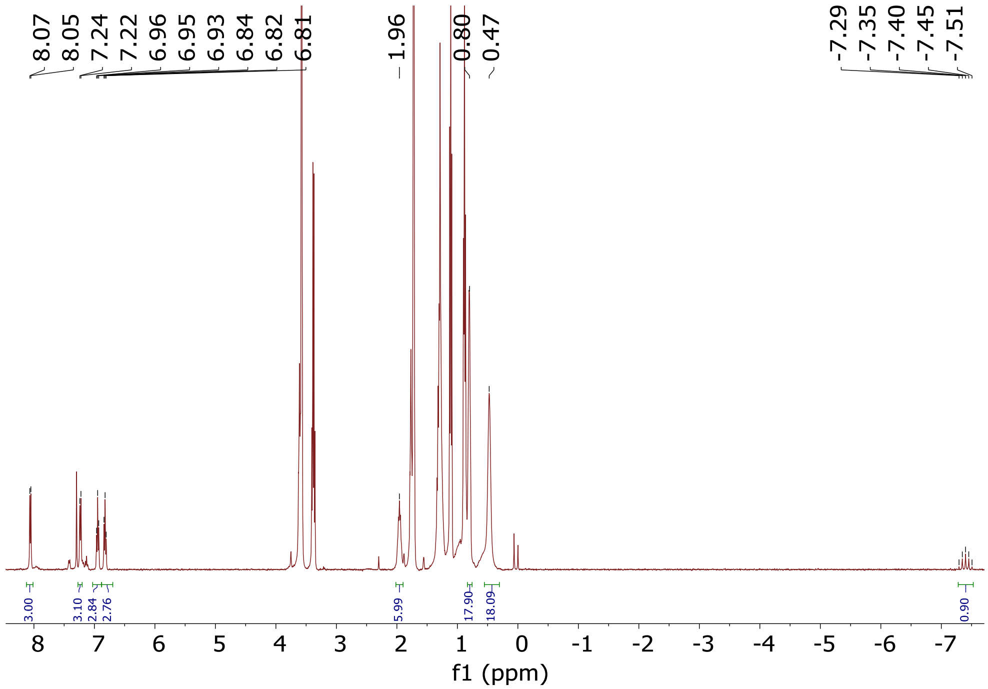

Figure S4. ^{1}H NMR (400 MHz, d_8-THF, 295 K) of Rh–H complex **5**. Peaks left unanalyzed are from THF, pentane, benzene, HMDSO, and diethyl ether.

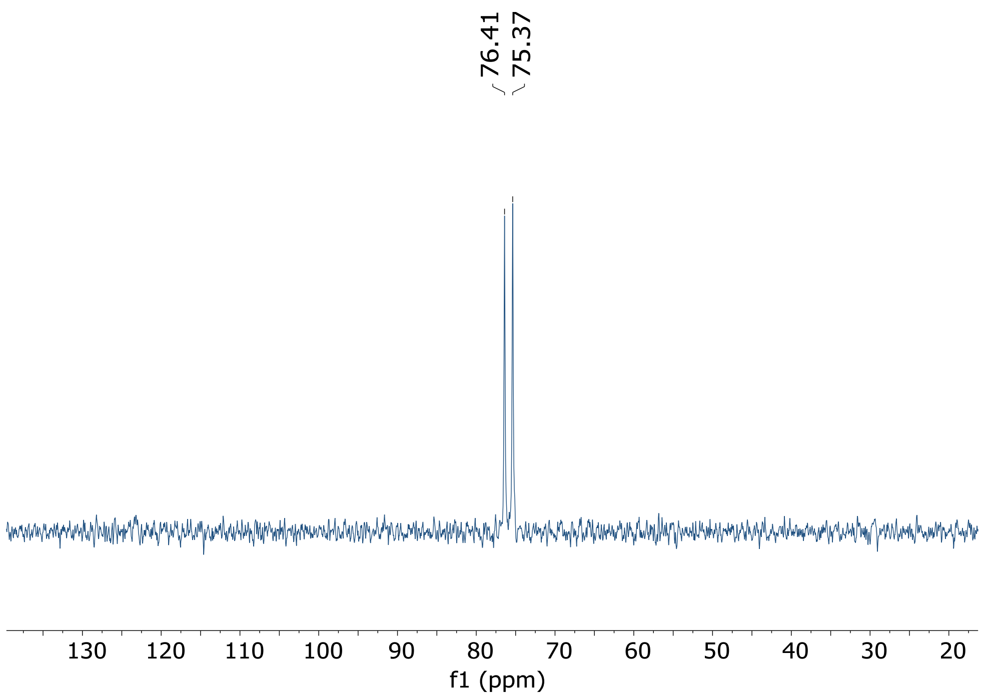

Figure S5. ^{31}P NMR (162 MHz, d_8-THF, 295 K) of Rh–H complex **5**.

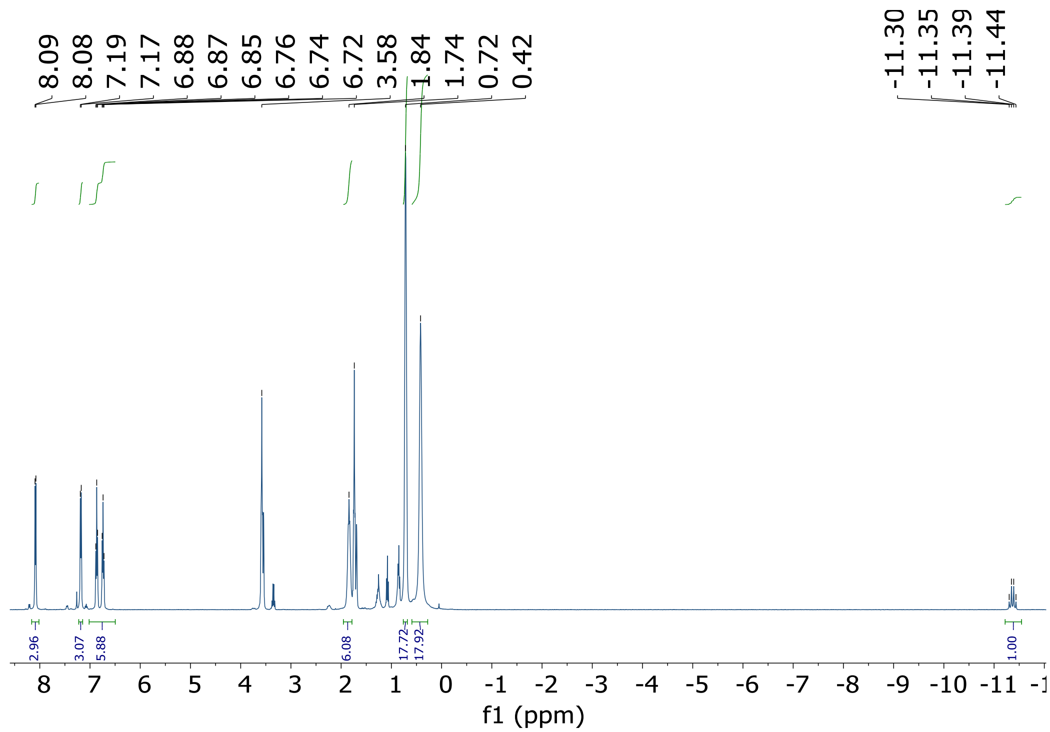

Figure S6. ^1H NMR (400 MHz, d$_8$-THF, 295 K) of complex **6** (Ir(I) hydride). Peaks left unanalyzed are from THF, pentane, and diethyl ether.

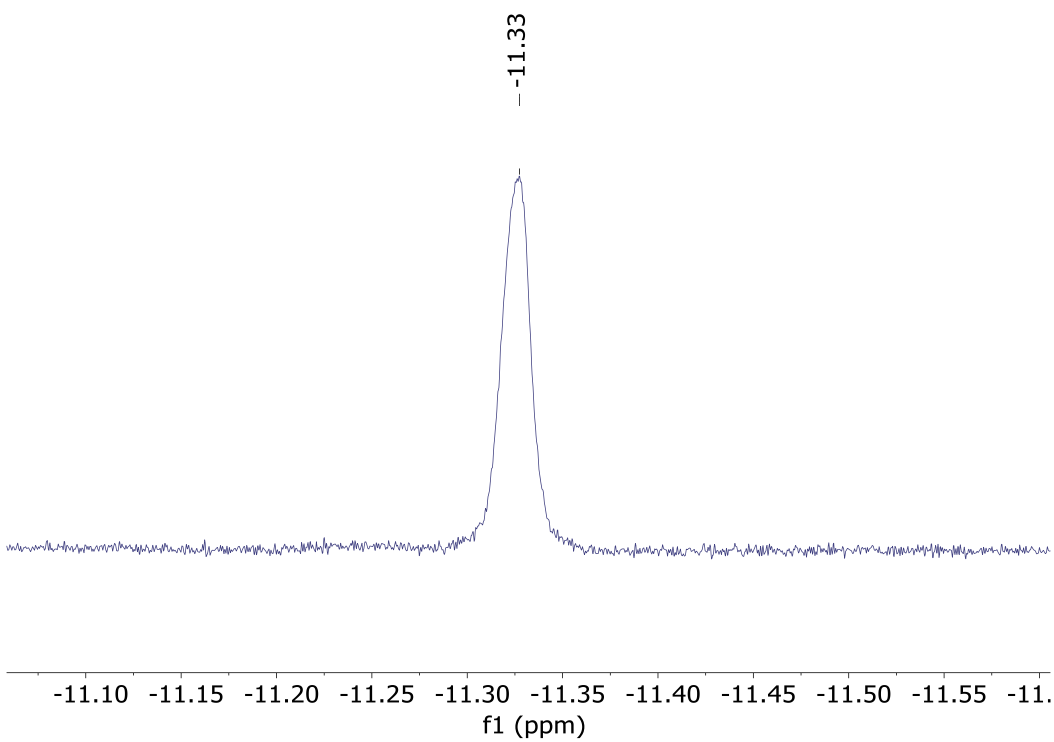

Figure S7. $^1H\{^{31}P\}$ NMR spectrum of complex **6** (Ir(I) hydride) at hydride resonance region.

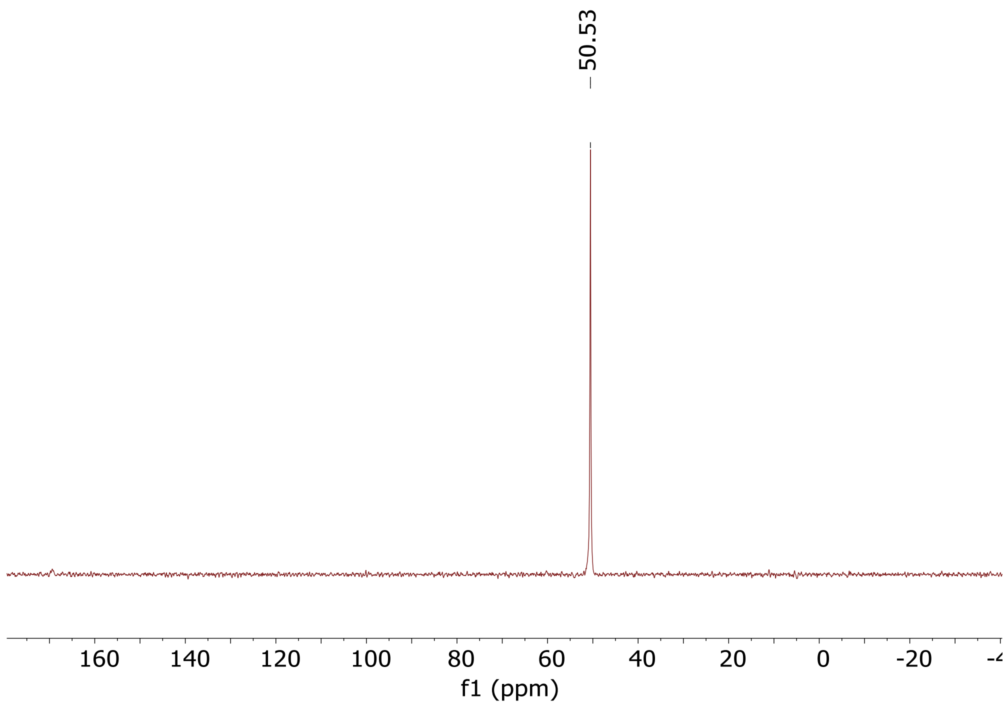

Figure S8. ^{31}P NMR (162 MHz, d_8-THF, 295 K) of complex **6** (Ir(I) hydride).

X-Ray diffraction

Table S1. Crystallographic data for complex **3**.

Empirical formula	$C_{48}H_{78}KO_3P_3RhSi$ (**3**)
Formula weight	966.12
Temperature/K	100(2)
Crystal system	Trigonal
Space group	*R3*
a/Å	18.001(2)
b/Å	18.001(2)
c/Å	13.8761(18)
α/°	90
β/°	90
γ/°	120
Volume/Å^3	3893.9(10)
Z	2.99997
ρ_{calc}g/cm^3	1.236
μ/mm^{-1}	4.745
F(000)	1539.0
Crystal size/mm^3	0.16 × 0.12 × 0.02
Radiation	CuKα (λ = 1.54178)

2Θ range for data collection/°	8.53 to 159.316
Index ranges	$-22 \leq h \leq 22$, $-20 \leq k \leq 22$, $-17 \leq l \leq 16$
Reflections collected	19219
Independent reflections	3543 [R_{int} = 0.0500, R_{sigma} = 0.0376]
Data/restraints/parameters	3543/172/177
Goodness-of-fit on F^2	1.127
Final R indexes [I>=2σ (I)]	R_1 = 0.0491, wR_2 = 0.1286
Final R indexes [all data]	R_1 = 0.0516, wR_2 = 0.1314
Largest diff. peak/hole / e $Å^{-3}$	1.60/-1.11
Flack parameter	0.192(18)

This crystal was refined as a 2-component inversion twin. The following twin law was obtained using Olex2: TWIN LAW (-1.0, 0.0, 0.0, 0.0, -1.0, 0.0, 0.0, 0.0, -1.0), BASF [0.192(18)]. Bond metrics are shown below with the DFT optimized structures.

Table S2. Crystallographic data for complex **4**.

Empirical formula	$C_{48}H_{78}IrKO_3P_3Si$
Formula weight	1055.41
Temperature/K	100.0
Crystal system	trigonal
Space group	R3
a/Å	18.085(3)
b/Å	18.085
c/Å	12.718(4)
α/°	90
β/°	90
γ/°	120
Volume/$Å^3$	3602.4(17)
Z	2.99997
ρ_{calc}g/cm^3	1.459
μ/mm^{-1}	3.030
F(000)	1635.0
Crystal size/mm^3	0.14 × 0.10 × 0.04
Radiation	MoKα (λ = 0.71073)
2Θ range for data collection/°	6.11 to 80.766
Index ranges	$-32 \leq h \leq 32$, $-32 \leq k \leq 32$, $-22 \leq l \leq 23$
Reflections collected	85559
Independent reflections	9884 [R_{int} = 0.0512, R_{sigma} = 0.0465]
Data/restraints/parameters	9884/1/181
Goodness-of-fit on F^2	1.028
Final R indexes [I>=2σ (I)]	R_1 = 0.0245, wR_2 = 0.0349

Final R indexes [all data]	R_1 = 0.0268, wR_2 = 0.0353
Largest diff. peak/hole / e Å^{-3}	2.80/-0.94
Flack parameter	0.044(3)

This crystal was co-crystallized with some of Ir-hydride complex **6**, as complex **4** reacts slowly with THF to give the Ir-hydride product. Bond metrics are shown below with the DFT optimized structures.

Table S3. Crystallographic data for complex **5**.

Empirical formula	$C_{48}H_{79}KO_3P_3RhSi$ (**5**)
Formula weight	967.13
Temperature/K	100(2)
Crystal system	Trigonal
Space group	*R3*
a/Å	18.184(4)
b/Å	18.184(4)
c/Å	12.679(3)
α/°	90
β/°	90
γ/°	120
Volume/Å^3	3630.7(17)
Z	2.99997
ρ_{calc}g/cm^3	1.327
μ/mm^{-1}	0.601
F(000)	1542.0
Crystal size/mm^3	0.25 × 0.21 × 0.1
Radiation	MoKα (λ = 0.71073)
2Θ range for data collection/°	6.928 to 112.434
Index ranges	$-41 \le h \le 40$, $-42 \le k \le 42$, $-29 \le l \le 29$
Reflections collected	208843
Independent reflections	21246 [R_{int} = 0.0359, R_{sigma} = 0.0250]
Data/restraints/parameters	21246/1/178
Goodness-of-fit on F^2	1.021
Final R indexes [I>=2σ (I)]	R_1 = 0.0207, wR_2 = 0.0427
Final R indexes [all data]	R_1 = 0.0237, wR_2 = 0.0437
Largest diff. peak/hole / e Å^{-3}	0.98/-0.55
Flack parameter	-0.006(2)

The hydride electron density was located in the difference map for this structure.

Table S4. Bond metrics for Rh–H **5**

d(Rh–K)	4.0850(9)
d(Rh–H)	1.70(3)
d(H–K)	2.39(3)
d(Rh–Si)	2.2702(5)
d(Rh–P1)	2.2814(5)
d(Rh–P2)	2.2814(5)
d(Rh–P3)	2.2814(5)
∠Si–Rh–P1	83.096(4)
∠P1–Rh–P2	118.576(2)
∠P2–Rh–P3	118.576(2)
∠P1–Rh–P3	118.577(2)
∠K–Rh–Si	180.0

*Discussion of the location of the K^+ cation in the structures of **3** and **4**.*

The M–K distances (3.495(4) Å for Rh and 3.483(5) Å for Ir) fall within the sum of the van der Waals radii of the atoms, which is between 4.5 and 5.0 Å depending on the values used.[8] After obtaining the structures, we wondered if there was any degree of TM^-–K^+ covalent bonding in these complexes. Thus, Löwdin spin populations (TPSS, ZORA scalar relativistic treatment, def2-SVP on all atoms except Rh, Ir (def2-QZVP) and Si, P (def2-TZVP); geometry optimizations performed from nuclear coordinates obtained via XRD) were calculated, both including and omitting the $[K(THF)_3]^+$ counterions. When the K^+ cation is included, approximately 20% of an electron is predicted to reside in K-based orbitals for both complexes. To investigate whether such behavior can be observed in solution and thus might contribute to the stability of the zerovalent species, we took advantage of the three NMR active isotopes of potassium (^{39}K, ^{40}K, ^{41}K), reasoning that if such a degree of TM^-–K^+ covalency were present *in solution*, there would be a change in the CW EPR spectra of **3** and **4** upon removing the K counterion (thereby removing any K hyperfine coupling interaction). First, solutions of **3** and **4** were mixed with benzo-15-crown-5 in an attempt to complex the K^+ cation and hinder any interaction with the Rh/Ir anion. However, this resulted in no change to the observed CW EPR spectra (Figure S9). To further rule out the possibility of a TM^-–K^+ in solution, a THF solution of lithium naphthalenide ($LiC_{10}H_8$) was prepared and reacted stoichiometrically with Rh/Ir–N_2 complexes **1** and **2** to generate the lithium analogues of **3** and **4**. Again, no changes are observed in the CW EPR spectra for either case, implying the EPR traces do not reflect coupling to K^+ (or Li^+), suggesting that in solution **3** and **4** behave as separated ion pairs (see below). As an additional control, an analogous experiment was performed but using $NaC_{10}H_8$ as the reductant; again, no change in the EPR spectrum was observed. The solid-state CW EPR spectra of **3** and **4** are quite broad and do not show easily-interpretable hyperfine coupling patterns. Additionally, solid-state relaxation times in the solid-state proved too fast for analysis by pulse EPR spectroscopy. We therefore cannot reliably comment on the degree, if any, of TM$^-$-K$^+$ covalency in the solid-state. For our DFT calculations, the $[K(THF)_3]^+$ cation has been omitted to reflect the behavior of **3** and **4** in solution.

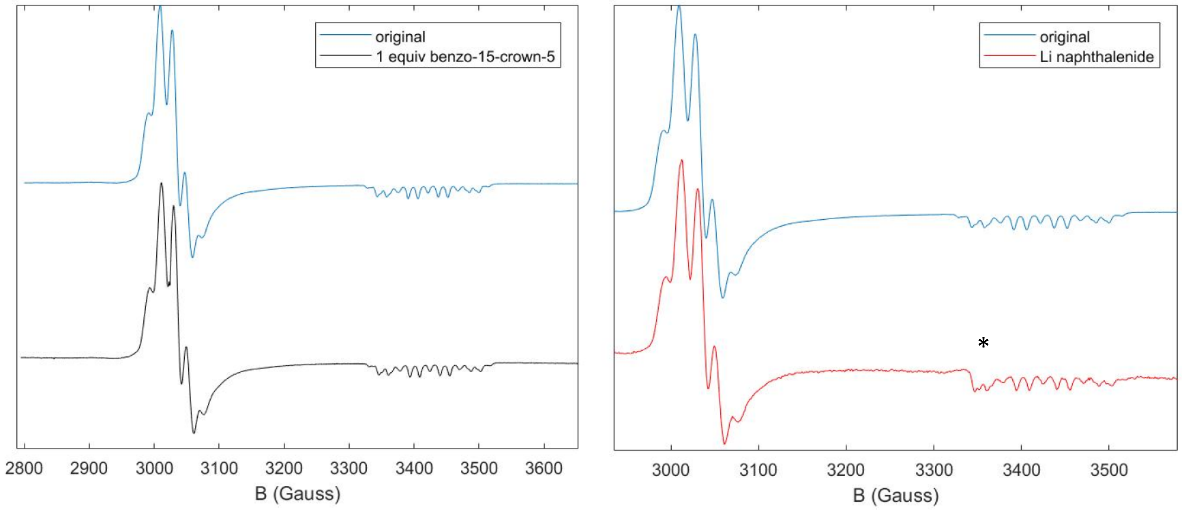

Figure S9. 77 K CW EPR spectrum of (left) **4** with and without benzo-15-crown-5 present, and (right) **4** generated either with KC_8 (top trace) or with $LiC_{10}H_8$ (bottom trace). *denotes a small amount of unreacted $LiC_{10}H_8$ that appears at the free-electron *g*-value.

HYSCORE spectra

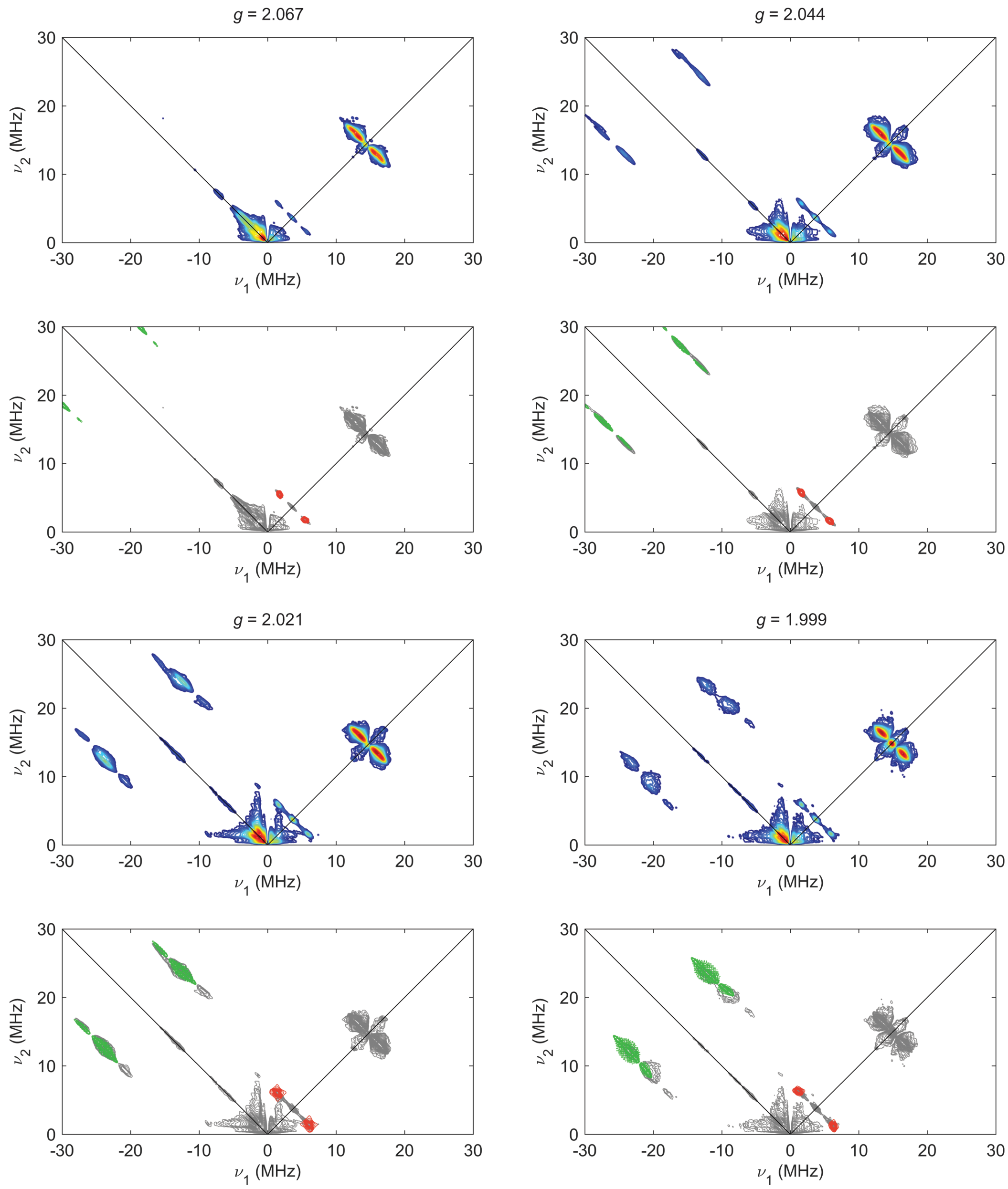

Figure S10. Field-Dependent X-Band HYSCORE spectra of $[P_3^{Si}Rh]^-$ **3** (top) with comparison (bottom) of experimental data (grey) to simulations of ^{31}P (green) and natural abundance ^{13}C (green) with A = [3.2, 3.2, 5.8] MHz. Intense correlation ridges in the (+,+) quadrant centered on the diagonal at c.a. 14 MHz arise from weakly coupled protons of the ligand or solvent matrix. Acquisition parameters: Temperature = 35 K; microwave frequency = 9.738 GHz; τ = 140 ns (g = 2.067), τ = 138 ns (g = 2.044), τ = 136 ns (g = 2.021), τ = 136 ns (g = 1.999); $t_1 = t_2$ = 100 ns; $\Delta t_1 = \Delta t_2$ = 16 ns; shot repetition time (srt) = 1 ms).

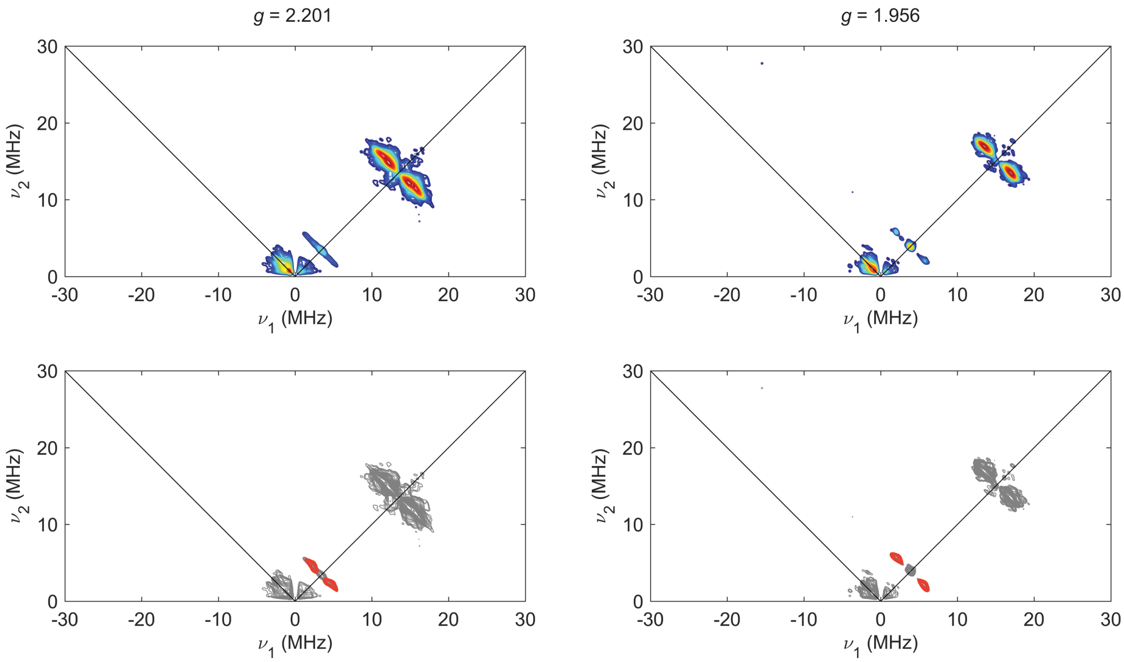

Figure S11. Field-Dependent X-Band HYSCORE spectra of $[P_3^{Si}Ir]^-$ **4** (top) with comparison (bottom) of experimental data (grey) to simulations of natural abundance ^{13}C (green) with A = [1.0, 1.0, 5.0] MHz. Intense correlation ridges in the (+,+) quadrant centered on the diagonal at c.a. 14 MHz arise from weakly coupled protons of the ligand or solvent matrix. Acquisition parameters: Temperature = 12 K; microwave frequency = 9.734 GHz; τ = 148 ns (g = 2.201), τ = 132 ns (g = 1.956); $t_1 = t_2$ = 100 ns; $\Delta t_1 = \Delta t_2$ = 16 ns; shot repetition time (srt) = 1 ms).

UV/Vis spectra

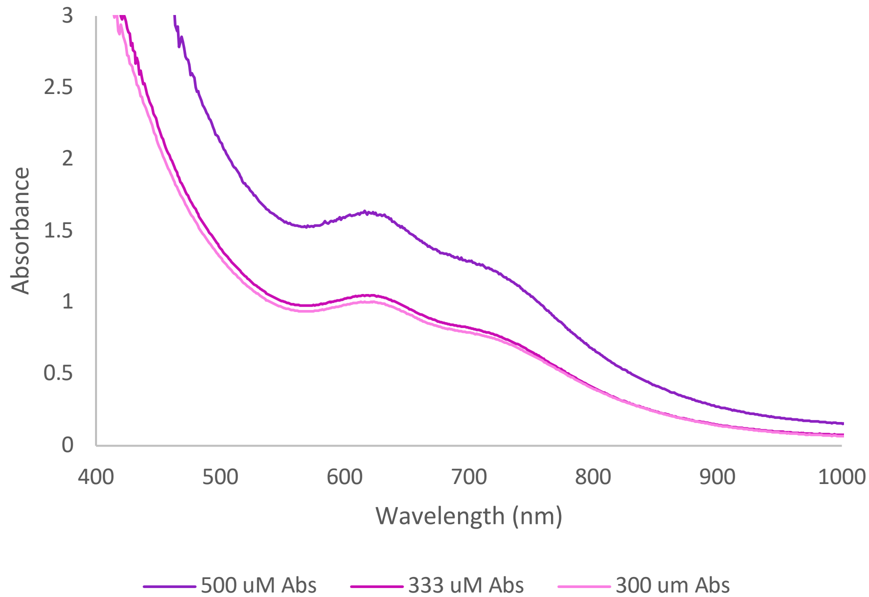

Figure S12. Visible spectrum of $[P_3^{Si}Rh]^-$ **3** at varying concentrations.

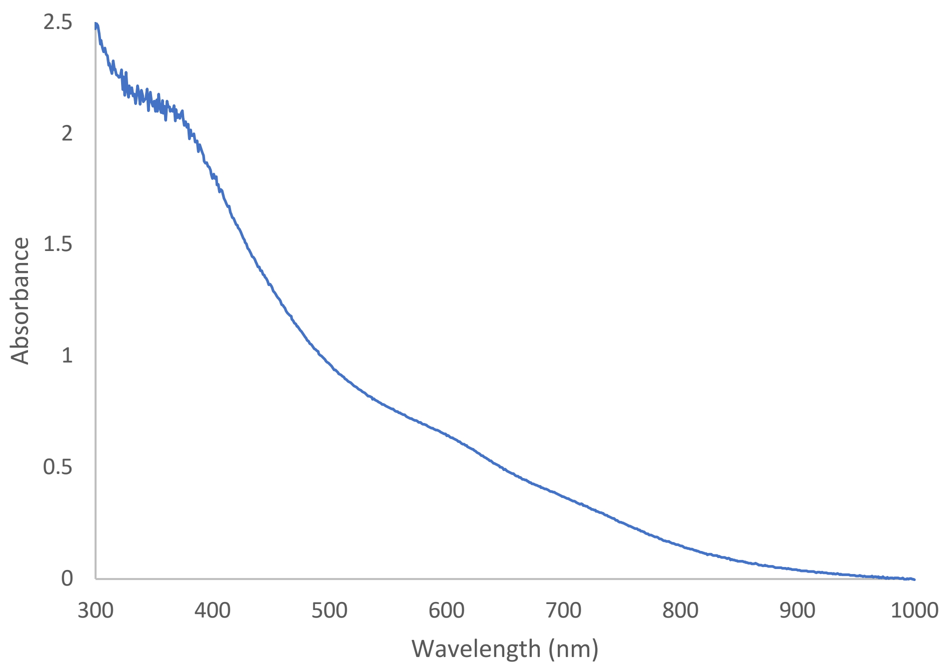

Figure S13. Visible spectrum of $[P_3^{Si}Ir]^-$ **3** at 190 μM.

Cyclic voltammograms

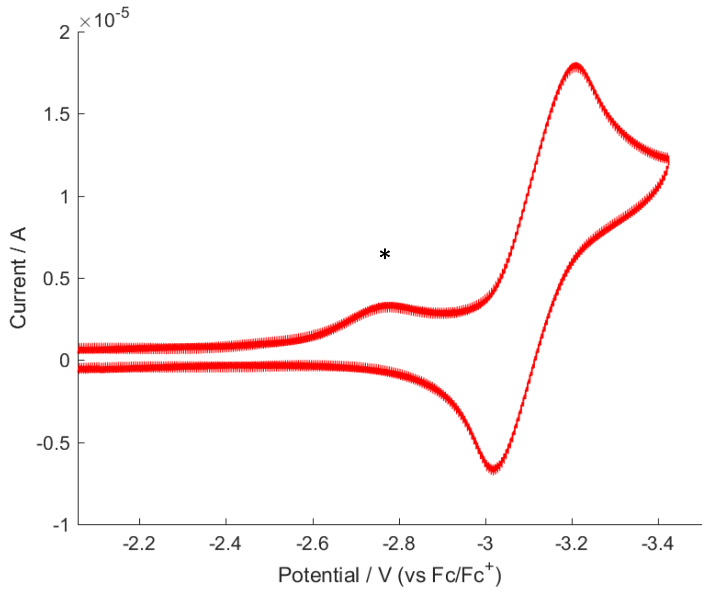

Figure S14. Cyclic voltammogram of $[P_3^{Si}Rh]^-$ **3** (scanned cathodically). Asterisks denotes minor impurity. Scan rate = 100 mV/s.

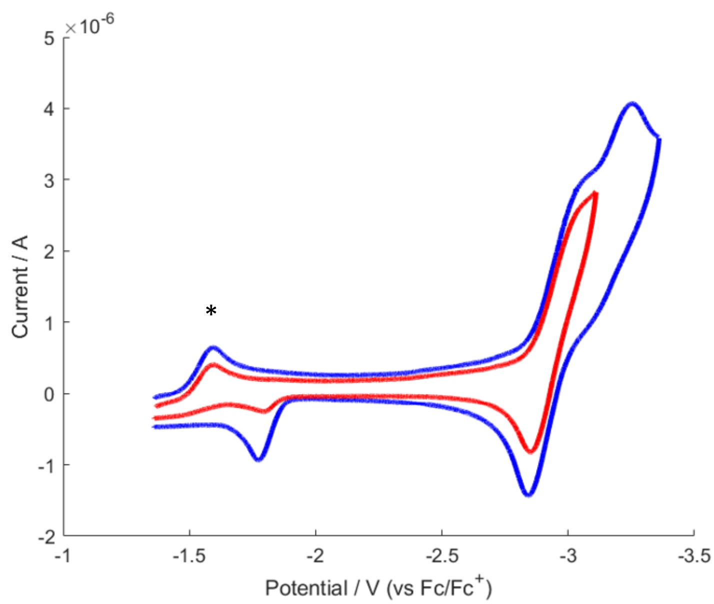

Figure S15. Cyclic voltammogram of Ir complex **4** (scanned cathodically). Asterisks denotes minor impurity. The oxidation wave at ~ −1.8 V is associated with the product of the irreversible reduction that occurs at ~ −3.3 V, as shown by the decrease in intensity in the red trace. Scan rate = 100 mV/s.

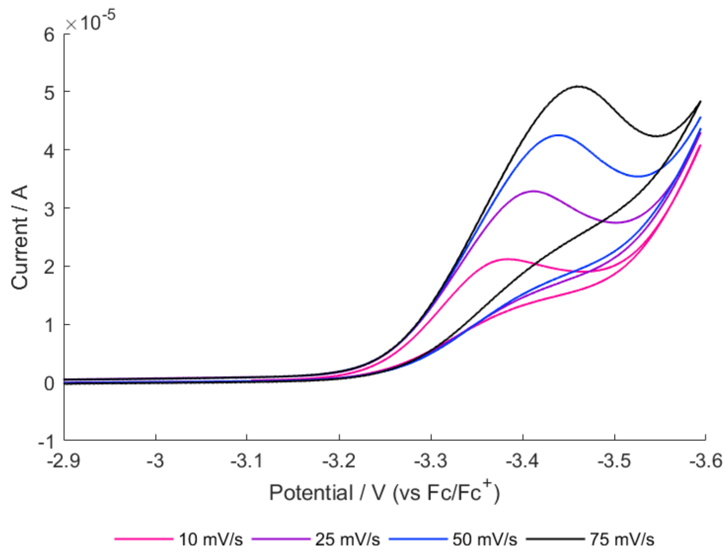

Figure S16. Cyclic voltammograms of $P_3^{Si}CoN_2$ at several scan rates. Scanned cathodically.

DFT calculations

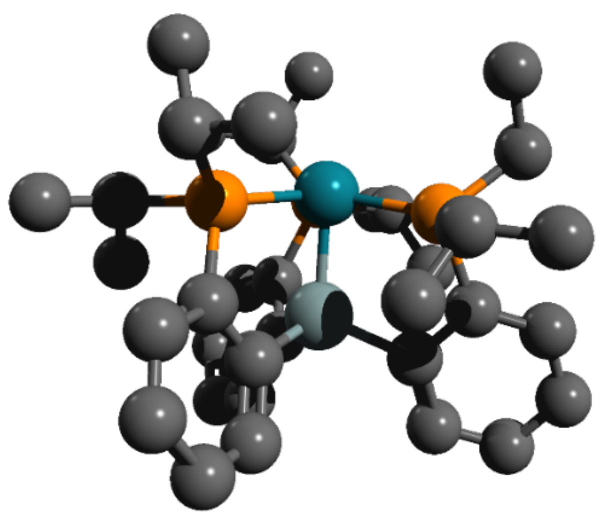

Figure S17. Pictorial depiction of DFT optimized geometry $[P_3^{Si}Rh]^-$ **3.**

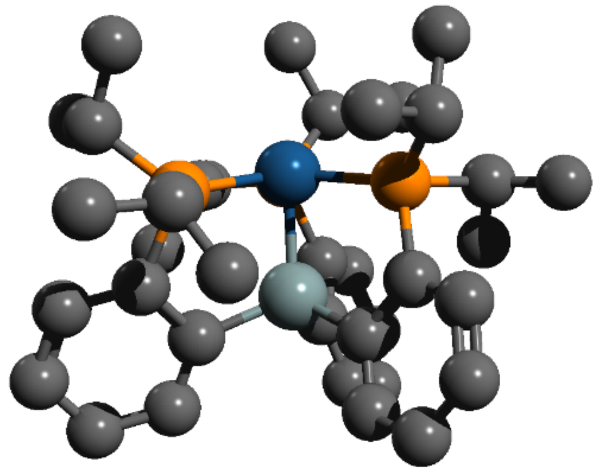

Figure S18. Pictorial depiction of DFT optimized geometry of $[P_3^{Si}Ir]^-$ **3**.

Table S5. Bond Metrics from XRD and DFT[a]

	Rh (**3**) XRD	Rh (**3**) DFT	Ir (**4**) XRD	Ir (**4**) DFT
d(M–K)	3.495(4)	not calculated	3.483(5)	not calculated
d(M–Si)	2.239(3)	2.240	2.2666(10)	2.2483
d(M–P1)	2.2908(15)	2.2799	2.2696(5)	2.2614
d(M–P2)	2.2909(15)	2.2801	2.2696(6)	2.2610
d(M–P3)	2.2909(15)	2.2785	2.2697(4)	2.2605
∠Si–M–P1	84.05(5)	84.51	83.980(12)	85.010
∠P1–M–P2	118.938(16)	119.100	118.915(10)	119.357
∠P2–M–P3	118.937(16)	119.211	118.912(5)	119.173
∠P1–M–P3	118.936(17)	118.981	118.916(12)	119.301
∠K–M–Si	180.0	not calculated	180.0	not calculated

[a]All distances are shown in Å and angles are shown in degrees.

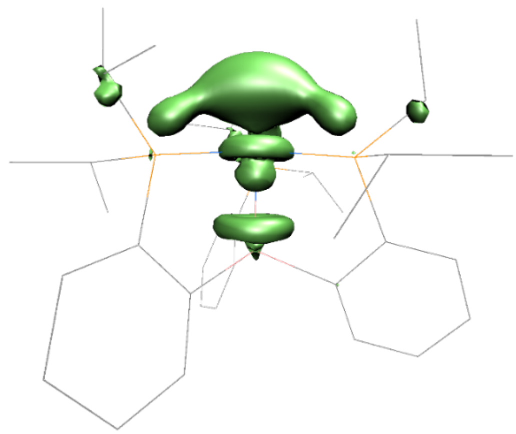

Figure S19. Contour plot of the spin density of $[P_3^{Si}Rh]^-$ (**3**). Isovalue = 0.003 a.u.

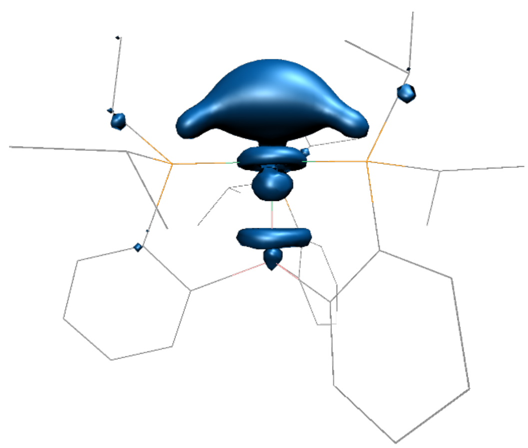

Figure S20. Contour plot of the spin density of $[P_3^{Si}Ir]^-$ (**4**). Isovalue = 0.003 a.u.

Table S6. Composition of the SOMO for $[P_3^{Si}Rh]^-$ (**3**) and $[P_3^{Si}Ir]^-$ (**4**) as calculated with TPSS method.

	$P_3^{Si}Rh^-$		$P_3^{Si}Ir^-$
Rh	43.9%[a] (4.6% s, 25.1% p_z, 14.2% d_{z^2})	Ir	47.8% (2.8% s, 31.7% p_z, 13.3% d_{z^2})
Si	10.4% (1.7% s, 8.7% p_z)	Si	8.5% (1.4% s, 7.1% p_z)
P1	5.5% (2.5% p_z, 3.0% d_{xz})	P1	4.6% (2.2% p_z, 2.4% d_{yz})
P2	4.7% (2.5% p_z, 2.2% d_{yz})	P2	4.8% (2.2% p_z, 2.6% d_{yz})
P3	4.8% (2.5% p_z, 2.3% d_{xz})	P3	5.5% (2.2% p_z, 3.3% d_{xz})

[a]1.0% was used as a cut off for summing orbital contributions.

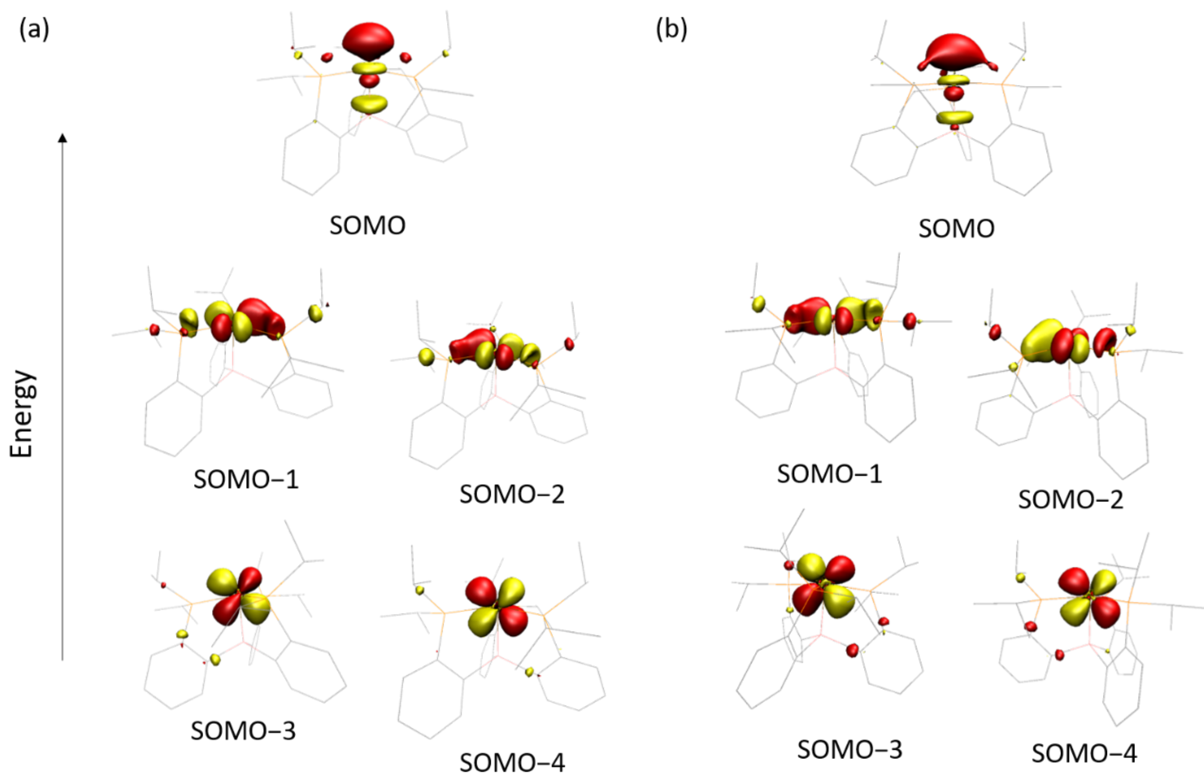

Figure S21. Contour plots of the DFT calculated frontier molecular orbitals of $[P_3^{Si}Rh]^-$ (**3**) and $[P_3^{Si}Ir]^-$ (**4**). Alpha spin orbitals are shown. Isovalue = 0.06 a.u.

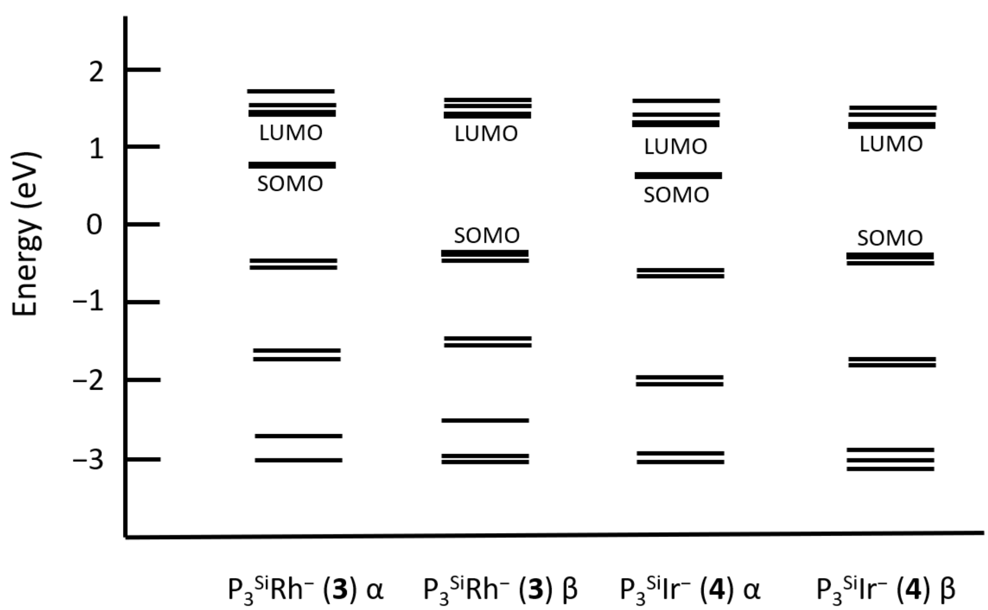

Figure S22. DFT calculated molecular orbital energy diagrams for $[P_3^{Si}Rh]^-$ (**3**) and $[P_3^{Si}Ir]^-$ (**4**).

Table S7. DFT calculated orbital energies for $[P_3^{Si}Rh]^-$ (**3**)

$P_3^{Si}Rh^-$ α			$P_3^{Si}Rh^-$ β		
Orbital	Orbital #	Energy (eV)	Orbital	Orbital #	Energy (eV)
SOMO−6[a]	181	−3.0481	SOMO−6	180	−3.0289
SOMO−5	182	−2.8580	SOMO−5	181	−3.0282
SOMO−4	183	−1.8377	SOMO−4	182	−2.7102
SOMO−3	184	−1.8352	SOMO−3	183	−1.7241
SOMO−2	185	−0.5496	SOMO−2	184	−1.7220
SOMO−1	186	−0.5436	SOMO−1	185	−0.4433
SOMO	187	0.8716	SOMO	186	−0.4370
LUMO	188	1.4601	LUMO	187	1.4614
LUMO+1	189	1.4643	LUMO+1	188	1.4805
LUMO+2	190	1.7557	LUMO+2	189	1.4849

[a]Alpha and beta orbitals were used because **3** is open shell, so all occupied orbitals are singly occupied.

Table S8. DFT calculated orbital energies for $[P_3^{Si}Ir]^-$ (**4**)

$P_3^{Si}Ir^-$ α			$P_3^{Si}Ir^-$ β		
Orbital	Orbital #	Energy (eV)	Orbital	Orbital #	Energy (eV)
SOMO−6[a]	197	−3.0807	SOMO−6	196	−3.0666
SOMO−5	198	−2.9518	SOMO−5	197	−3.0653
SOMO−4	199	−2.0048	SOMO−4	198	−2.9065
SOMO−3	200	−2.0024	SOMO−3	199	−1.8774
SOMO−2	201	−0.6002	SOMO−2	200	−1.8753
SOMO−1	202	−0.5840	SOMO−1	201	−0.5055
SOMO	203	0.7461	SOMO	202	−0.4897
LUMO	204	1.4481	LUMO	203	1.4202
LUMO+1	205	1.4522	LUMO+1	204	1.4651
LUMO+2	206	1.7412	LUMO+2	205	1.4695

[a]Alpha and beta orbitals were used because **4** is open shell, so all occupied orbitals are singly occupied.

Table S9. Optimized coordinates for $[P_3^{Si}Rh]^-$ **3**.

Rh	9.00127	5.19604	8.19128
P	6.97316	4.18127	8.41138
Si	9.00320	5.19520	10.43106
C	6.75231	2.27821	8.52970
H	7.21420	1.92004	7.59586
C	5.38209	5.34061	12.67543
H	5.04242	5.63669	13.67136
C	5.31435	1.73503	8.60211
H	4.80311	2.09482	9.50768
H	5.33360	0.63221	8.65276
H	4.70538	2.01158	7.72917
C	7.57431	1.73467	9.70717
H	8.60024	2.11704	9.68677
H	7.61513	0.63339	9.67799
H	7.12932	2.03544	10.66763
C	6.26248	4.61908	10.08869
C	6.75387	5.32232	12.37154
H	7.47200	5.61754	13.14143
C	4.88917	4.62875	10.40380
H	4.14812	4.37258	9.64328
C	7.21624	4.98332	11.08396
C	5.34987	6.08224	7.11348
H	5.03120	6.51677	8.07078
H	4.58888	6.32623	6.35251
H	6.30298	6.55293	6.82743
C	5.90100	3.96960	5.84481
H	6.89184	4.33592	5.53013
H	5.15741	4.26890	5.08724
H	5.94053	2.86952	5.86450
C	4.44814	5.00277	11.68533
H	3.37765	5.03642	11.90497
C	5.54753	4.56539	7.22087
H	4.61512	4.10464	7.58671
P	10.89589	3.94612	8.40745
C	12.65386	4.70768	8.52335
H	12.73145	5.28604	7.58932
C	10.67829	1.97865	12.66679
H	10.58670	1.53313	13.66095
C	13.84288	3.73448	8.59545
H	13.78685	3.10936	9.49926
H	14.78862	4.30176	8.64868
H	13.91046	3.07045	7.72131
C	12.71431	5.69243	9.69868
H	11.86796	6.38796	9.68067
H	13.64677	6.28051	9.66521
H	12.68237	5.15951	10.66099
C	10.87237	3.11013	10.08390
C	10.01464	3.17983	12.36556
H	9.39983	3.65379	13.13614

C	11.54558	1.91262	10.39668
H	12.13623	1.39882	9.63509
C	10.08072	3.75318	11.07989
C	10.06212	1.58958	7.10575
H	9.84027	1.09695	8.06266
H	10.23447	0.80819	6.34678
H	9.17870	2.17928	6.81597
C	11.61796	3.12389	5.84114
H	10.80537	3.79813	5.52339
H	11.73471	2.32949	5.08504
H	12.54914	3.70899	5.86358
C	11.43630	1.33868	11.67562
H	11.93380	0.39001	11.89107
C	11.27655	2.51991	7.21628
H	12.14100	1.94202	7.58328
P	9.13218	7.46092	8.40859
C	7.58975	8.59789	8.52302
H	7.04628	8.36603	7.59361
C	10.93598	8.26309	12.67066
H	11.36512	8.40876	13.66525
C	7.82936	10.11672	8.58216
H	8.40251	10.39101	9.48111
H	6.86278	10.64570	8.63689
H	8.36348	10.50363	7.70261
C	6.71508	8.16415	9.70826
H	6.53957	7.08274	9.70019
H	5.73885	8.67396	9.67793
H	7.19878	8.41371	10.66494
C	9.86417	7.86012	10.08659
C	10.23888	7.08137	12.36661
H	10.14197	6.30905	13.13565
C	10.55416	9.04782	10.40163
H	10.69730	9.81878	9.64101
C	9.71061	6.84996	11.08079
C	11.59905	7.94225	7.12876
H	12.12824	8.01690	8.08910
H	12.18683	8.48205	6.36746
H	11.54762	6.87779	6.85066
C	9.49599	8.47961	5.83953
H	9.34491	7.43335	5.52647
H	10.12098	8.98796	5.08636
H	8.51284	8.97192	5.85009
C	11.10174	9.24371	11.68171
H	11.66225	10.15606	11.90062
C	10.17637	8.50840	7.22141
H	10.22634	9.54858	7.58116

Table S10. Optimized coordinates for $[P_3^{Si}Ir]^-$ **3.**

Ir	9.04945	5.22579	5.72507
Si	9.04701	5.22713	3.47680
P	7.19126	6.50048	5.53460
C	5.42806	5.74889	5.43969
H	5.36337	5.16545	6.37102
C	6.83069	7.91861	6.73761
H	5.96199	8.49556	6.37965
C	8.04214	8.85182	6.84516
H	8.92517	8.26464	7.13964
H	7.86634	9.63447	7.60202
H	8.26525	9.34263	5.88765
C	5.34402	4.77257	4.25927
H	5.35520	5.31251	3.30041
H	4.41345	4.18274	4.30814
H	6.19184	4.07845	4.25609
C	7.96770	6.67566	2.84458
C	7.20028	7.32909	3.85354
C	6.53010	8.52986	3.54934
H	5.95850	9.05046	4.32075
C	7.34753	8.44654	1.26192
H	7.42113	8.88607	0.26364
C	8.00921	7.24183	1.55546
H	8.60298	6.75939	0.77374
C	6.50277	7.30629	8.11260
H	5.57398	6.71737	8.09571
H	6.38916	8.09709	8.87299
H	7.32113	6.63366	8.41857
C	4.24238	6.72820	5.39402
H	4.18834	7.38122	6.27717
H	3.29381	6.16527	5.34579
H	4.28869	7.36445	4.49732
C	6.61672	9.09737	2.26572
H	6.12210	10.04891	2.05638
P	8.87739	2.97961	5.53177
C	10.41387	1.83362	5.43985
H	10.95425	2.07984	6.36688
C	7.82872	1.95343	6.72935
H	7.78496	0.90953	6.38033
C	6.40353	2.51226	6.81440
H	6.44976	3.57595	7.09368
H	5.81639	1.96967	7.57417
H	5.87727	2.43516	5.85275
C	11.29384	2.24340	4.25056
H	10.81644	1.97087	3.29706
H	12.27187	1.73841	4.29763
H	11.46499	3.32570	4.23748
C	8.50553	2.00225	8.11268
H	9.49176	1.51617	8.11130
H	7.88107	1.49863	8.86949

H	8.64951	3.05349	8.41195
C	10.16814	0.31461	5.40731
H	9.63665	-0.05531	6.29568
H	11.13269	-0.21843	5.35804
H	9.59085	0.02595	4.51547
C	8.33491	3.56800	2.84222
C	8.16048	2.57240	3.84843
C	7.46782	1.38507	3.54049
H	7.30940	0.62616	4.31012
C	7.12661	2.13735	1.25471
H	6.71256	1.97953	0.25565
C	7.82604	3.31975	1.55245
H	7.94063	4.07897	0.77293
C	6.93856	1.17331	2.25525
H	6.37575	0.26119	2.04129
P	11.08161	6.19619	5.52868
C	11.31359	8.09873	5.43009
H	10.84078	8.44862	6.36118
C	12.49096	5.79981	6.73019
H	13.42393	6.26608	6.37330
C	12.69457	4.28425	6.83358
H	11.74491	3.81154	7.12572
H	13.45990	4.04336	7.59115
H	13.00968	3.85025	5.87500
C	10.51032	8.65812	4.24775
H	10.97132	8.37196	3.29028
H	10.46673	9.75872	4.29199
H	9.48485	8.27335	4.24806
C	12.12308	6.38639	8.10685
H	12.07942	7.48637	8.09438
H	12.86146	6.08480	8.86862
H	11.13047	6.01421	8.40861
C	12.75531	8.63590	5.38346
H	13.34785	8.35508	6.26619
H	12.74122	9.73890	5.33560
H	13.28120	8.27711	4.48586
C	10.84039	5.43602	2.83935
C	11.79208	5.77320	3.84690
C	13.16657	5.75683	3.54002
H	13.90471	5.99272	4.30991
C	12.68174	5.09512	1.25215
H	13.02443	4.81562	0.25253
C	11.30799	5.11984	1.54857
H	10.59231	4.84755	0.76790
C	13.61243	5.40342	2.25424
H	14.68396	5.36355	2.04072

References

1. Whited, M. T.; Mankad, N. P.; Lee, Y.; Oblad, P. F.; Peters, J. C. *Inorg. Chem.* **2009**, *48*, 2507–2517.
2. Takaoka, A.; Peters, J. C. *Inorg. Chem.* **2012**, *51*, 16–18.
3. Weitz, I. S.; Rabinovitz, M. *J. Chem. Soc., Perkin Trans. 1* **1993**, 117.
4. Neese, F. *Wiley Interdisciplinary Reviews: Computational Molecular Science* **2012**, *2*, 73-78.
5. Neese, F. *WIREs Comput Mol Sci* **2018***,* 8:e1327. doi: 10.1002/wcms.1327.
6. Stoll, S., Schweiger, A. (2006) EasySpin, a comprehensive software package for spectral simulations and analysis in EPR. *J. Mag. Reson.* **178**, 42-55.
7. Hyde, J. S., Pasenkiewicz-Gierula, M., Jesmanowicz, A., Antholine, W. E., (1990) Pseudo field modulation in EPR spectroscopy. *Appl. Mag. Reson*. **1**, 483-496.
8. Batsanov, S. S. *Inorganic Materials*, **2001**, *37*, 871–885.